2.13
Failure of Functionally Graded Materials

G. H. PAULINO, Z.-H. JIN, and R. H. DODDS, Jr.
University of Illinois, Urbana, USA

2.13.1 INTRODUCTION

Many future advancements in science and technology will rely heavily upon the development of new material systems that safely withstand the ever-increasing performance demands imposed upon them. Functionally graded materials (FGMs) hold promise for applications requiring ultrahigh material performance such as thermal barrier coatings, bone and dental implants, piezoelectric and thermoelectric devices, optical materials with graded reflective indices, and high-performance spaceflight structures (including engines). New applications are continuously being discovered.

FGMs are characterized by spatially varied microstructures created by nonuniform distributions of the reinforcement phase with different properties, sizes and shapes, as well as by interchanging the role of reinforcement and matrix (base) materials in a continuous manner as illustrated by Figure 1. This new concept of engineering the microstructure of the material marks the beginning of a paradigm shift in the way we think about materials and structures as it allows one, due to recent advances in material processing, to fully integrate material and structural design considerations.

2.13.1.2 Background

The initial response to provide materials that accommodate nonhomogeneous service requirements employed layered structures, e.g., coatings (Kaczmarek *et al.*, 1984; Suganuma *et al.*, 1984). However, under severe stress gradients, such structures proved susceptible to failure from spalling triggered by high interfacial stresses. In contrast, FGMs make possible stress relaxation under the imposed thermomechanical loads. This is accomplished by providing a compositional distribution function, $C(x)$, consistent with these conditions. For instance, such a function can be expressed as (Hirano *et al.*, 1990)

$$C(x) = (C_2 - C_1)\left(\frac{x - x_1}{x_2 - x_1}\right)^n \qquad (1)$$

where C_1 and C_2 denote composition values at opposite ends of the FGM layer corresponding to the distances x_1 and x_2, respectively. Figure 2 illustrates this function. The exponent n in Equation (1) dictates the nature of the desired distribution function based on stress analyses. For example, in FGMs of TiC/Ni, Ma *et al.* (1992) report that the optimum value for n lies in the range 0.5–0.7. Thus, to accommodate the desired distribution function, the method of FGM manufacturing must have the capability to provide the predetermined (desired) exponent n (see Equation (1) and Figure 2).

FGMs possess the distinguishing feature of nonhomogeneity with regard to their thermomechanical and strength-related properties including yield strength, fracture toughness, fatigue, and creep behavior (see, e.g., Erdogan,

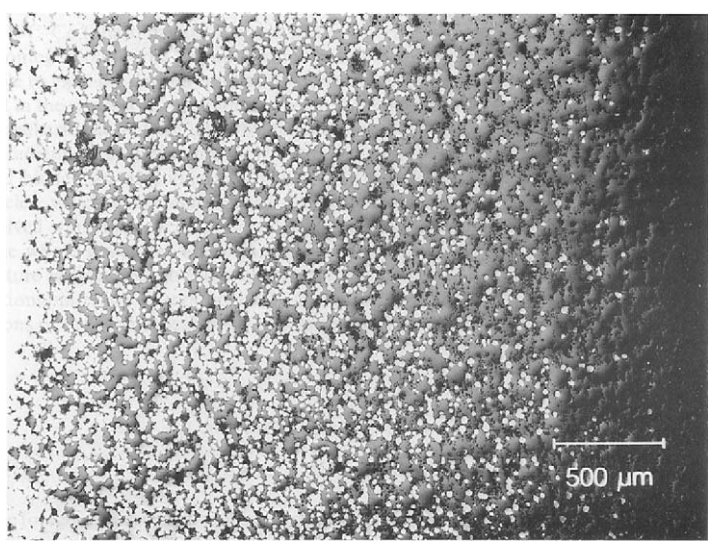

Figure 1 Transition in a CrNi/PSZ FGM from CrNi alloy to zirconia (PSZ) (after Ilschner, 1996).

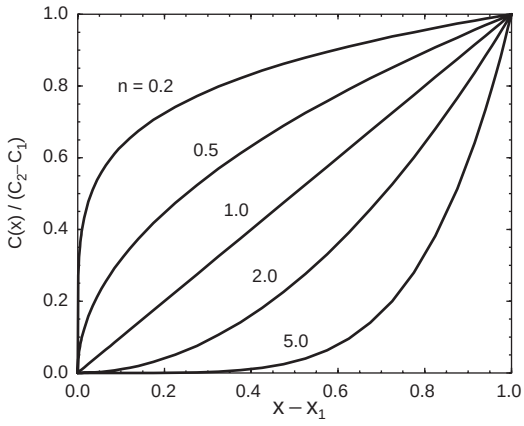

Figure 2 Plot of the normalized composition function $C(x)$ versus $x-x_1$ for selected values of n with $x_1 = 1.0$ and $x_2 = 2.0$—see Equation (1).

1995; Paulino and Jin, 2001a). Numerous investigators have developed theoretical and numerical fracture mechanics models for FGMs (Noda and Jin, 1993; Bao and Wang, 1995; Giannakopoulos *et al*., 1995; Lee and Erdogan, 1995; Choi, 1996a, 1996b; Jin and Batra, 1996c; Bao and Cai, 1997; Ozturk and Erdogan, 1997; Gu and Asaro, 1997a; Chan *et al*., 2001). Yang and Shih (1994) have studied the fracture process along a nonhomogeneous interlayer between two dissimilar materials. Jin and Batra (1996a) have presented a micromechanics-based model of fracture toughness. Erdogan (1995) and Markworth *et al*. (1995) have presented complementary reviews of modeling techniques applied to FGMs. Noda (1999) has written an extensive review on thermal stresses in FGMs. Pindera *et al*. (1998) have presented a thermomechanical analysis of functionally graded thermal barrier coatings with different microstructural scales. Jin *et al*. (2002) presented a cohesive zone model to simulate progressive material failure and crack extension in FGMs coupled with some experimental validation.

This work presents a comprehensive review on fracture/failure of FGMs. Several relevant aspects of the above mentioned papers are discussed in detail. Moreover, the presentation that follows integrates aspects such as processing, experiments, theory/analysis, and modeling/simulation.

2.13.1.3 Processing and Manufacturing of FGMs

Modeling and design of FGMs should be considered in conjunction with synthesis techniques—thus a few remarks about materials processing are in order. Details of processing technologies can be found, e.g., in Hirai (1996), and Suresh and Mortensen (1998). The fabrication of FGMs include, e.g., vapor phase (e.g., chemical vapor deposition: CVD, physical vapor deposition: PVD), liquid phase (e.g., sol–gel, plasma, spraying), and solid phase (e.g., self-propagating high-temperature synthesis: SHS, powder stacking) methods (Hirai, 1996). In the SHS method, a variety of modifications have been used to obtain dense products (Miyamoto *et al*., 1992; Sata, 1993). An important advantage of the SHS method relative to other powder processing methods lies in its short duration. A developed approach, known as field activated combustion synthesis (FACS) (Munir *et al*., 1995; Feng and Munir, 1994, 1995a, 1995b; Xue and Munir, 1995, 1997; Munir, 1996, 1997), has been shown to improve the performance of previous SHS methods. In FACS, an electric field is applied during combustion to synthesize materials which cannot be prepared by SHS, e.g., SiC, B_4C, $MoSi_2$–SiC, etc. (Carrillo-Heian *et al*., 2001a, 2001b). Xue and Munir (1995) showed that FACS can extend the compositional limit in composites. Table 1 provides a summary of fabrication methods and examples of FGMs fabricated by these methods.

Table 1 Some fabrication methods and examples of FGMs.

Methods	*Examples*
Vapor phase methods	
CVD	SiC/C, SiC/TiC
CVI	SiC/C, TiB_2/SiC
Liquid phase methods	
Electro-depositing	Cu/CuZn, Cu/CuNi
Electro-plating	CoNiReP(f.c.c)/ CoNiReP(h.c.p.)
Plasma spraying	PSZ/SS, PSZ/NiCrAl
Centrifugal casting	SiC/Al
Solid phase methods	
(a) Powder stacking methods	
Centrifugal	ZrO_2/NiCr
Spraying	PSZ/SS
Filtration	Al_2O_3/Ni
Sedimentation	Al_2O_3/NiAl, $A1_2O_3$/W
(b) Sintering methods	
Sintering, HP and HIP	PSZ/SS, Al_2O_3/Ni AlN/Ni, Si_3N_4/Mo
Plasma activated	PSZ/SS, PSZ/Ti
FACS	$MoSi_2$/SiC, Nb_5Si_3/Nb
SHS	TiB_2/Cu, TiB_2/Ni
SPS	ZrO_2/SUS401L
Diffusion and reaction	PZT/NiNb Al_2O_3/Sn/Nb/Sn/Al_2O_3

2.13.2 MECHANICS MODELS OF FGMs

2.13.2.1 Continuum Model

From the continuum mechanics point of view, FGMs are nonhomogeneous materials, i.e., the material properties of an FGM, e.g., Young's modulus (E), Poisson's ratio (ν), mass density (ρ), yield stress (σ_0), and tangent modulus (E_T), are functions of spatial position. This work focuses on FGMs undergoing elastic deformations governed by the equations of nonhomogeneous elastic materials (Fung, 1965). Those basic equations include the equation of motion

$$\sigma_{ij,\,j} = \rho(\boldsymbol{x})\frac{\partial^2 u_i}{\partial t^2} \tag{2}$$

the strain–displacement relation

$$\varepsilon_{ij} = \tfrac{1}{2}(u_{i,j} + u_{j,i}) \tag{3}$$

and the constitutive law

$$\varepsilon_{ij} = S_{ijkl}(\boldsymbol{x})\sigma_{kl} \tag{4}$$

in which σ_{ij} are stresses, ε_{ij} are strains, u_i are displacements, $\boldsymbol{x} = (x_1,\ x_2,\ x_3) = (x,\ y,\ z)$, $S_{ijkl}(\boldsymbol{x})$ are the compliance coefficients, $\rho(\boldsymbol{x})$ is the mass density, the Latin indices have the range 1, 2, 3, and repeated indices imply the summation convention. Under isotropic conditions, Equation (4) reduces to

$$\varepsilon_{ij} = \frac{1+\nu(\boldsymbol{x})}{E(\boldsymbol{x})}\sigma_{ij} - \frac{\nu(\boldsymbol{x})}{E(\boldsymbol{x})}\sigma_{kk}\delta_{ij} \tag{5}$$

where $E(\boldsymbol{x})$ is Young's modulus, $\nu(\boldsymbol{x})$ is Poisson's ratio, and δ_{ij} is the Kronecker delta. In the continuum analysis, E, ν, and other material properties (e.g., shear modulus) are continuous functions of the spatial coordinate $\boldsymbol{x}$. They can be calculated from a micromechanics model (see Section 2.13.2.2) or can be assumed to follow some elementary functions. An exponentially varying Young's modulus and a constant Poisson's ratio find frequent use in quasistatic crack problems (e.g., Konda and Erdogan, 1994). The benefit of using an exponential function for Young's modulus is that the final governing equations (e.g., Navier–Cauchy equations) for FGMs reduce to constant coefficient, partial differential equations that may be solved either analytically or semianalytically. Other commonly used functions include linear (e.g., Marur and Tippur, 1998; Kim and Paulino, 2002) and hyperbolic–tangent (e.g., Eischen, 1987a).

Now consider quasistatic, two-dimensional (2D) deformations of a nonhomogeneous material with the following properties:

$$\mu \equiv \mu(x,\ y) = \mu_0 \exp(\beta x + \gamma y), \quad \nu \equiv \nu_0 \tag{6}$$

where μ is the space-dependent shear modulus

$$\mu(x,\ y) = \frac{E(x,\ y)}{2(1+\nu)} \tag{7}$$

and μ_0, ν_0, β, and γ are material constants. The inverse of the parameters β and γ defines the length scale of material nonhomogeneity in the x- and y-directions, respectively. The Navier–Cauchy equations for the material with the properties Equation (6) are

$$\begin{aligned}
&(\kappa+1)\frac{\partial^2 u}{\partial x^2} + (\kappa-1)\frac{\partial^2 u}{\partial y^2} + 2\frac{\partial^2 v}{\partial x \partial y} \\
&\quad + \beta(\kappa+1)\frac{\partial u}{\partial x} + \gamma(\kappa-1)\frac{\partial u}{\partial y} + \gamma(\kappa-1)\frac{\partial v}{\partial x} \\
&\quad + \beta(3-\kappa)\frac{\partial v}{\partial y} = 0 \\
&(\kappa-1)\frac{\partial^2 v}{\partial x^2} + (\kappa+1)\frac{\partial^2 v}{\partial y^2} + 2\frac{\partial^2 u}{\partial x \partial y} \\
&\quad + \gamma(3-\kappa)\frac{\partial u}{\partial x} + \beta(\kappa-1)\frac{\partial u}{\partial y} + \beta(\kappa-1)\frac{\partial v}{\partial x} \\
&\quad + \gamma(\kappa+1)\frac{\partial v}{\partial y} = 0
\end{aligned} \tag{8}$$

where $u = u_1$, $v = u_2$, and $\kappa = 3-4\nu_0$ for plane strain, and $\kappa = (3-\nu_0)/(1+\nu_0)$ for plane stress. Notice that when $\beta \to 0$ and $\gamma \to 0$, the above equations reduce to the standard equations of homogeneous elasticity (Timoshenko and Goodier, 1973). Once the displacement solution is available, stresses are found simply by using Hooke's law

$$\begin{aligned}
\sigma_{xx} &= \frac{\mu_0 \exp(\beta x + \gamma y)}{\kappa - 1}\left[(\kappa+1)\frac{\partial u}{\partial x} + (3-\kappa)\frac{\partial v}{\partial y}\right] \\
\sigma_{yy} &= \frac{\mu_0 \exp(\beta x + \gamma y)}{\kappa - 1}\left[(\kappa+1)\frac{\partial v}{\partial y} + (3-\kappa)\frac{\partial u}{\partial x}\right] \\
\sigma_{xy} &= \mu_0 \exp(\beta x + \gamma y)\left(\frac{\partial u}{\partial y} + \frac{\partial v}{\partial x}\right)
\end{aligned} \tag{9}$$

2.13.2.2 Micromechanics Models

The material properties of an FGM, such as Young's modulus and Poisson's ratio, most often are evaluated from properties of the constituent materials using micromechanics models. Conventional composite models (Nemat-Nasser and Hori, 1993) generally apply when the volume fraction of one constituent in the FGM remains much smaller than that of the other. However, the validity of such models cannot be assured over the entire range of

material volume fractions; they rely on the spatial uniformity of constituent distributions and microstructure of the composite. The main feature of FGMs lies in the nonuniform microstructure with continuous change in volume fractions. In fact, micromechanics models widely applicable to FGMs remain largely unavailable (Zuiker, 1995). Dvorak and Zuiker (1994), Reiter *et al.* (1997), and Reiter and Dvorak (1998) have indicated that, among various micromechanics models for conventional composite materials, Mori–Tanaka and self-consistent models may be used to estimate the effective properties of graded materials with reasonable accuracy. However, a theoretical basis for such applications remains unclear because the concept of a representative volume element cannot be unique for FGMs in the presence of continuously graded properties. To overcome this limitation of standard micromechanics models in FGM applications, Aboudi *et al.* (1999) developed a higher-order micromechanical theory. The fundamental framework of the higher-order theory relies upon volumetric averaging of the various quantities, satisfaction of the field equations in a volumetric sense, and imposition in an average sense of boundary and interfacial conditions between the subvolumes to characterize the graded microstructures. A detailed description and discussion of the higher-order theory can be found in the review paper by Aboudi *et al.* (1999). Moreover, Section 2.13.2 of their paper provides insights on the application of micromechanics models (originally developed for conventional composites) to FGMs. Motivated by the above exposition, this section first reviews the self-consistent and Mori–Tanaka models. Then, a modified rule of mixture model proposed by Tamura *et al.* (1973) is discussed. Finally, the popular Hashin–Shtrikman bounds (Hashin and Shtrikman, 1963) are introduced.

2.13.2.2.1 Self-consistent model

The self-consistent method was first proposed to estimate the elastic properties of polycrystalline materials which, in fact, are just one phase media. Due to the random or partially random distribution of crystal orientation, discontinuities in properties exist across crystal interfaces. In the application to polycrystalline aggregates, a single anisotropic crystal is viewed as a spherical or ellipsoidal inclusion embedded in an infinite medium of the unknown isotropic properties of the aggregate. Then the system is subjected to uniform stress or strain conditions at large distances from the inclusion. Next the orientation average of the stress or strain in the inclusion is set equal to the corresponding applied value of the remote stress or strain. Thus the name "self-consistent" comes from this procedure.

When applying the self-consistent method to a two-phase composite, the shear and bulk moduli μ and K of the composite have the following forms (Hill, 1965):

$$\frac{1}{K+(4/3)\mu}=\frac{V_1}{K_1+(4/3)\mu}+\frac{V_2}{K_2+(4/3)\mu} \tag{10}$$

$$\left(\frac{V_1K_1}{K_1+(4/3)\mu}+\frac{V_2K_2}{K_2+(4/3)\mu}\right)+5\left(\frac{V_1\mu_2}{\mu-\mu_2}+\frac{V_2\mu_1}{\mu-\mu_1}\right)+2=0 \tag{11}$$

where V_1 and V_2 are the volume fractions of phase 1 and phase 2, respectively, μ_1 and μ_2 are the shear moduli of phase 1 and phase 2, respectively, and K_1 and K_2 are the bulk moduli of phase 1 and phase 2, respectively. Once the above nonlinear equations are solved for μ and K, Young's modulus E and Poisson's ratio v of the composite are then determined from the following elasticity relations:

$$E=\frac{9\mu K}{\mu+3K},\quad v=\frac{3K-2\mu}{2(\mu+3K)} \tag{12}$$

2.13.2.2.2 Mori–Tanaka model

Like the self-consistent method, the Mori–Tanaka method also uses the average local stress and strain fields in the constituents of a composite to estimate the effective material properties of the composite. The Mori–Tanaka method (Mori and Tanaka, 1973), however, involves rather complicated manipulations of the field variables along with the concepts of eigenstrain, backstress, etc. Later, Benveniste (1987) provided a more direct and simplified derivation of the Mori–Tanaka method.

The Mori–Tanaka estimates of the effective shear and bulk moduli μ and K of a two-phase composite with spherical inclusion were derived by Benveniste (1987) as follows:

$$\mu=\mu_1+V_2(\mu_2-\mu_1)\times\left\{1+V_1(\mu_2-\mu_1)\left[\mu_1+\frac{\mu_1(9K_1+8\mu_1)}{6(K_1+2\mu_1)}\right]^{-1}\right\} \tag{13}$$

$$K=K_1+V_2(K_2-K_1)\left\{1+V_1\left[\frac{K_2-K_1}{K_1+(4/3)\mu_1}\right]\right\}^{-1} \tag{14}$$

Once the above equations are evaluated for μ and K, Young's modulus E and Poisson's ratio v are given by Equation (12).

2.13.2.2.3 Tamura–Tomota–Ozawa model

Based on a rule of mixtures, Tamura *et al.* (1973) proposed a simple model (Tamura–Tomota–Ozawa (TTO) model) to describe the stress–strain curves of composite materials. Their model has been employed to study FGMs by Williamson *et al.* (1993), Giannakopoulos *et al.* (1995), and Carpenter *et al.* (1999). The TTO model couples the uniaxial stress (σ) and strain (ε) of the composite to the corresponding average uniaxial stresses and strains of the two constituent materials by

$$\sigma = V_1\sigma_1 + V_2\sigma_2, \quad \varepsilon = V_1\varepsilon_1 + V_2\varepsilon_2 \qquad (15)$$

where σ_i and ε_i ($i = 1, 2$) are the average stresses and strains of the constituent phases, respectively, and V_i ($i = 1, 2$) are volume fractions. The TTO model introduces an additional parameter, q, to represent the ratio of stress-to-strain transfer

$$q = \frac{\sigma_1 - \sigma_2}{\varepsilon_1 - \varepsilon_2}, \quad 0 < q < \infty \qquad (16)$$

It is clear that $q = 0$ and $q \to \infty$ correspond to property averaging with equal stress and equal strain, respectively. Young's modulus of the composite may be obtained from Equations (15) and (16) as

$$E = \left[V_2E_2\frac{q+E_1}{q+E_2} + (1-V_2)E_1\right] \times \left[V_2\frac{q+E_1}{q+E_2} + (1-V_2)\right]^{-1} \qquad (17)$$

where E_i ($i = 1, 2$) are Young's moduli of the basic constituent phases.

For applications of the TTO model to ceramic/metal (brittle/ductile) composites, the yield stress of the composite, σ_Y, is given by

$$\sigma_Y(V_2) = \sigma_{Y2}\left[V_2 + \frac{q+E_2}{q+E_1}\frac{E_1}{E_2}(1-V_2)\right] \qquad (18)$$

where σ_{Y2} is the yield stress of the metal (phase 2). Idealization of the metal as a bilinear material with a tangent modulus H_2 leads to a bilinear composite with the following tangent modulus H

$$H = \left[V_2H_2\frac{q+E_1}{q+H_2} + (1-V_2)E_1\right] \times \left[V_2\frac{q+E_1}{q+H_2} + (1-V_2)\right]^{-1} \qquad (19)$$

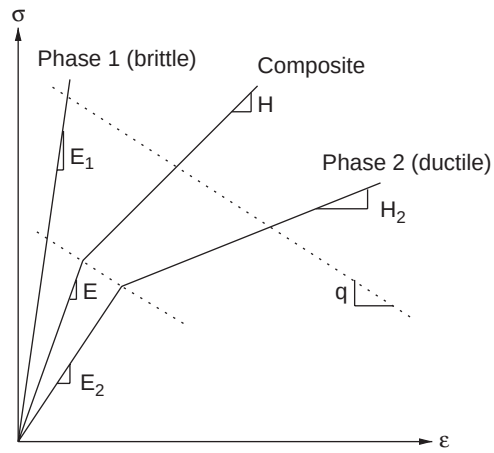

Figure 3 Schematic of the stress–strain curve for the TTO model.

Figure 3 shows the schematic of the stress–strain curve of the composite described by the TTO model.

When the metal follows a power-law relation with an exponent n_2, the following nonlinear equations determine the stress–strain curve for the composite

$$\frac{\varepsilon}{\varepsilon_Y} = \frac{V_1E}{q+E_1}\frac{\sigma_2}{\sigma_Y} + \frac{(q+V_2E_1)E}{(q+E_1)E_2}\frac{\sigma_{Y2}}{\sigma_Y}\left(\frac{\sigma_2}{\sigma_{Y2}}\right)^{n_2}$$
$$\frac{\sigma}{\sigma_Y} = \frac{V_2q+E_1}{q+E_1}\frac{\sigma_2}{\sigma_{Y2}} + \frac{V_1qE_1}{(q+E_1)E_2}\frac{\sigma_{Y2}}{\sigma_Y}\left(\frac{\sigma_2}{\sigma_{Y2}}\right)^{n_2} \qquad (20)$$

where $\varepsilon_{Y2} = \sigma_{Y2}/E_2$ and $\varepsilon_Y = \sigma_Y/E$ denote the yield strains of the metal and the composite, respectively. The constant q in the TTO model governs the interaction of the constituents in an FGM. In applications, q may be approximately determined by experimental calibration.

2.13.2.2.4 Hashin–Shtrikman bounds

Because effective properties of a composite material are estimated from micromechanics models such as the self-consistent and Mori–Tanaka models discussed above, it is important to provide bounds for those material properties. For a two-phase composite material, Hashin and Shtrikman (1963) derived the following bounds for the effective shear and bulk moduli

$$\mu_1^* = \mu_1 + V_2\left\{\frac{1}{\mu_2-\mu_1} + \frac{6(K_1+2\mu_1)V_1}{5\mu_1(3K_1+4\mu_1)}\right\}^{-1}$$
$$\mu_2^* = \mu_2 + V_1\left\{\frac{1}{\mu_1-\mu_2} + \frac{6(K_2+2\mu_2)V_2}{5\mu_2(3K_2+4\mu_2)}\right\}^{-1}$$
$$K_1^* = K_1 + V_2\left\{\frac{1}{K_2-K_1} + \frac{3V_1}{(3K_1+4\mu_1)}\right\}^{-1}$$
$$K_2^* = K_2 + V_1\left\{\frac{1}{K_1-K_2} + \frac{3V_2}{(3K_2+4\mu_2)}\right\}^{-1} \qquad (21)$$

where μ_1^* and K_1^* are the lower bounds, and μ_2^* and K_2^* are the upper bounds of the shear and bulk moduli, respectively, when $K_2 > K_1$, $\mu_2 > \mu_1$.

2.13.3 FRACTURE OF FGMs

2.13.3.1 Crack-tip Fields

As discussed in Section 2.13.2.1, FGMs are nonhomogeneous materials from the viewpoint of continuum mechanics, i.e., Young's modulus, E, and Poisson's ratio, v, of an FGM vary with spatial position. Eischen (1987a) studied the asymptotic crack-tip fields in general nonhomogeneous materials by using the traditional eigenfunction expansion technique as employed by Williams (1957). He has shown that the stress field angular functions associated with the first two terms (i.e., $r^{-1/2}$ and r^0) are not affected by the material property variation, and the effect of nonhomogeneity is reflected in higher order terms (i.e., $r^{1/2}$ and higher). However, explicit forms of the higher-order terms were not given. Parameswaran and Shukla (2002) have provided the first six terms of the stress field for a stationary crack, aligned along the gradient, in a material with exponentially graded E and constant v. They used an asymptotic analysis coupled with Westergaard's stress function approach.

When E and v are sufficiently smooth functions, Eischen (1987a) showed that the 2D crack-tip elastic fields remain identical to those in homogeneous materials. When E and v are not sufficiently smooth functions, i.e., they are continuous but only piecewise continuously differentiable (e.g., for a graded layer bonded to a homogeneous substrate), Jin and Noda (1994a) obtained the same result and further pointed out that the result can be extended to 3D, anisotropic, and elastic–plastic cases. Therefore, the asymptotic crack-tip stress and displacement fields in FGMs can be written as (Eischen, 1987a; Jin and Noda, 1994a)

$$\sigma_{\alpha\beta}(r,\theta) = \frac{1}{\sqrt{2\pi r}}\left\{K_{\mathrm{I}}\tilde{\sigma}_{\alpha\beta}^{(1)}(\theta) + K_{\mathrm{II}}\tilde{\sigma}_{\alpha\beta}^{(2)}(\theta)\right\}, \quad r \to 0 \tag{22}$$

$$u_{\alpha}(r,\theta) = \frac{1}{\mu_{\mathrm{tip}}}\sqrt{\frac{r}{2\pi}}\left\{K_{\mathrm{I}}\tilde{u}_{\alpha}^{(1)}(\theta) + K_{\mathrm{II}}\tilde{u}_{\alpha}^{(2)}(\theta)\right\}, \quad r \to 0 \tag{23}$$

where α, $\beta = 1$, 2, $\sigma_{\alpha\beta}$ are stresses, u_α are displacements, (r, θ) are the polar coordinates centered at the crack tip, K_{I} and K_{II} are mode I and mode II stress intensity factors (SIFs), respectively, $\tilde{\sigma}_{\alpha\beta}^{(1)}(\theta)$ and $\tilde{\sigma}_{\alpha\beta}^{(2)}(\theta)$ are standard angular distribution functions of stresses, $\tilde{u}_{\alpha}^{(1)}(\theta)$ and $\tilde{u}_{\alpha}^{(2)}(\theta)$ are standard angular distribution functions of displacements, and μ_{tip} is the shear modulus at the crack tip. Many textbooks on fracture list the standard angular functions, e.g., Anderson (1995). The singular parts of the crack-tip stresses in a material with the properties in Equation (6), as used by Erdogan (1995), are also given by Equation (22). Under plane-stress conditions, the crack-tip energy release rate, G, is related to the SIFs by

$$G = \frac{1}{E_{\mathrm{tip}}}(K_{\mathrm{I}}^2 + K_{\mathrm{II}}^2) \tag{24}$$

where $1/E_{\mathrm{tip}}$ is replaced by $(1 - v_{\mathrm{tip}}^2)/E_{\mathrm{tip}}$ in the above equation for plane-strain conditions. In Equation (24), E_{tip} and v_{tip} denote Young's modulus and Poisson's ratio at the crack tip, respectively.

2.13.3.2 Stress Intensity Factors

The assessment of crack-like defects and damage in FGMs requires SIF solutions for various crack problems. Extensive efforts have been made in recent years to obtain SIF solutions. This section reviews and discusses some available SIF solutions for cracks in nonhomogeneous materials. Emphasis is placed on analytical/semianalytical techniques for solving crack problems of nonhomogeneous materials. Section 2.13.4 discusses the computation of SIF solutions via numerical methods, e.g., finite element methods (FEMs).

2.13.3.2.1 Mechanical loads

The singular integral equation technique is a powerful analytical/semianalytical method to solve crack problems of nonhomogeneous materials (Chan *et al.*, 2003). A number of crack problems in FGMs have been studied using this method. For example, Delale and Erdogan (1983) studied a crack in an infinite FGM plate with a shear modulus that varies exponentially in the crack direction, which is a special case ($\theta = 0$) of the problem discussed below. For radial multiple-crack problems, Shbeeb *et al.* (1999a, 1999b) proposed a fundamental solution and performed a parametric study of SIFs. Delale and Erdogan (1988) have also considered a crack in an FGM layer between two dissimilar homogeneous half planes. Erdogan *et al.* (1991) studied a crack problem in bonded nonhomogeneous materials. Choi *et al.* (1998a) considered collinear cracks in a layered half plane with an FGM interlayer. Choi (2001a) studied an

inclined crack in an FGM layer between two dissimilar homogeneous half planes. Erdogan and Wu (1997) considered a crack in a finite-width FGM plate under tension, bending and fixed-grip displacement loads, respectively. Gu and Asaro (1997a) calculated SIFs for a semi-infinite crack in an FGM strip. Kadioglu *et al.* (1998) studied a crack problem for an FGM layer on an elastic foundation. Erdogan and Ozturk (1995), Chen and Erdogan (1996), and Jin and Batra (1996c) investigated cracks in FGM coatings. Ozturk and Erdogan (1997, 1999) investigated both mode I and mixed-mode crack problems in a nonhomogeneous orthotropic medium. Wang *et al*. (1997) studied a penny-shaped crack in a nonhomogeneous layer between dissimilar materials. Chan *et al.* (2001) investigated the crack problem for FGMs under antiplane shear loading by means of a displacement-based formulation leading to a hypersingular integral equation formulation. Besides the integral-equation technique, Fett *et al.* (2000) used a weight function method to calculate SIFs for FGMs.

We now describe a singular integral equation approach to obtain the SIFs for a crack in an infinite nonhomogeneous medium as shown in Figure 4. The shear modulus and Poisson's ratio follow the functional form

$$\mu \equiv \mu(x_1) = \mu_0 \exp(\delta x_1), \quad \nu \equiv \nu_0 \tag{25}$$

where μ_0, ν_0, and δ are material constants. The above expression shows that the shear modulus varies exponentially along an arbitrary x_1-direction. A crack of length $2a$ exists along the x-direction, which is inclined by angle θ from the x_1-direction (see Figure 4). This is a mixed-mode crack problem studied by Konda and Erdogan (1994). In the (x, y) coordinate

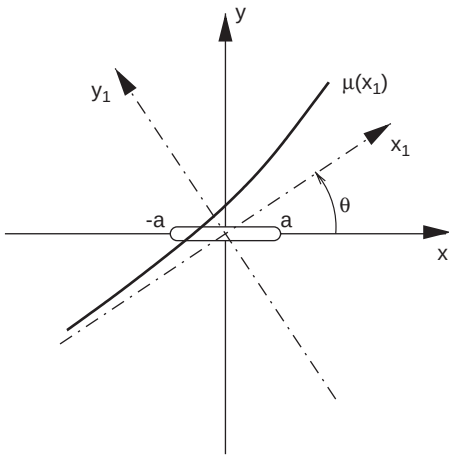

Figure 4 Crack geometry in nonhomogeneous medium (free space).

system, the shear modulus and Poisson's ratio have the form given by Equation (6)

$$\mu \equiv \mu(x, y) = \mu_0 \exp(\beta x + \gamma y), \quad \nu \equiv \nu_0$$

where β and γ are related to δ and θ by

$$\beta = \delta \sin\theta, \quad \gamma = \delta \cos\theta \tag{26}$$

The Navier–Cauchy equations for the material with the properties of Equation (25) are given in Equation (8). The boundary conditions of the crack problem can be formulated as

$$\begin{aligned} \sigma_{yy}(x, +0) &= p_1(x), \quad |x| < a \\ v(x, +0) &= v(x, -0), \quad |x| > a \end{aligned} \tag{27}$$

$$\begin{aligned} \sigma_{xy}(x, +0) &= p_2(x), \quad |x| < a \\ u(x, +0) &= u(x, -0), \quad |x| > a \end{aligned} \tag{28}$$

$$\begin{aligned} \sigma_{yy}(x, +0) &= \sigma_{yy}(x, -0) \\ \sigma_{xy}(x, +0) &= \sigma_{xy}(x, -0), \quad |x| < \infty \end{aligned} \tag{29}$$

By means of a Fourier transform, the boundary value problem, Equation (8) and Equations (27)–(29), reduces to the following system of singular integral equations

$$\begin{aligned} &\int_{-1}^{1} \left[\frac{f_2(s)}{s-r} + \sum_{j=1}^{2} L_{1j}(r, s) f_j(s) \right] \mathrm{d}s \\ &\quad = \frac{1+\kappa}{2\mu(r, 0)} p_1(r), \quad |r| < 1 \\ &\int_{-1}^{1} \left[\frac{f_1(s)}{s-r} + \sum_{j=1}^{2} L_{2j}(r, s) f_j(s) \right] \mathrm{d}s \\ &\quad = \frac{1+\kappa}{2\mu(r, 0)} p_2(r), \quad |r| < 1 \end{aligned} \tag{30}$$

where the unknown density functions $f_1(r)$ and $f_2(r)$ are the slopes of the crack displacement profile defined by

$$\begin{aligned} f_1(x) &= \frac{\partial}{\partial x}[u(x, +0) - u(x, -0)] \\ f_2(x) &= \frac{\partial}{\partial x}[v(x, +0) - v(x, -0)] \end{aligned} \tag{31}$$

respectively, the nondimensional coordinate r is

$$r = x/a \tag{32}$$

and the Fredholm kernels $L_{ij}(r, s)$ $(i, j = 1, 2)$ can be found in Konda and Erdogan (1994). In addition, the functions $f_1(r)$ and $f_2(r)$ satisfy the uniqueness conditions

$$\int_{-1}^{1} f_1(r)\, \mathrm{d}r = 0, \quad \int_{-1}^{1} f_2(r)\, \mathrm{d}r = 0 \tag{33}$$

To obtain the numerical solution of the system of governing integral Equation (30), the density functions, $f_1(r)$ and $f_2(r)$, are expanded into series of Chebyshev polynomials as follows:

$$f_1(r) = \frac{1}{\sqrt{1-r^2}} \sum_{n=1}^{\infty} A_n T_n(r), \quad |r| \le 1$$
$$f_2(r) = \frac{1}{\sqrt{1-r^2}} \sum_{n=1}^{\infty} B_n T_n(r), \quad |r| \le 1 \tag{34}$$

where $T_n(r)$ are Chebyshev polynomials of the first kind, and A_n and B_n are unknown constants. The functions $f_1(r)$ and $f_2(r)$ given by Equations (34) already satisfy the condition of Equations (33). By substituting Equation (34) into integral Equations (30), we have

$$\sum_{n=1}^{\infty} \{U_{n-1}(r) B_n + H_n^{11}(r) A_n + H_n^{12}(r) B_n\} = \frac{1+\kappa}{2\mu(r, 0)} p_1(r), \quad |r| \le 1$$
$$\sum_{n=1}^{\infty} \{U_{n-1}(r) A_n + H_n^{21}(r) A_n + H_n^{22}(r) B_n\} = \frac{1+\kappa}{2\mu(r, 0)} p_2(r), \quad |r| \le 1 \tag{35}$$

where $U_n(r)$ are Chebyshev polynomials of the second kind and $H_n^{ij}(r)$ $(i, j = 1, 2)$ are given by

$$H_n^{ij}(r) = \frac{1}{\pi} \int_{-1}^{1} L_{ij}(r, s) \frac{T_n(s)}{\sqrt{1-s^2}} \mathrm{d}s, \quad i, j = 1, 2 \tag{36}$$

To solve the functional Equations (35), the series on the left-hand side are first truncated at the Nth term. A collocation technique (Erdogan *et al.*, 1973; Erdogan, 1978) is then used and the collocation points, r_i, are chosen as the roots of the Chebyshev polynomials of the first kind

$$r_i = \cos \frac{(2i-1)\pi}{2N}, \quad i = 1, 2, \ldots, N \tag{37}$$

which are strategically selected such that more points are located closer to the crack tips than on the midregion of the crack surface. The SIFs at the crack tip $x = a$ are calculated from

$$K_{\mathrm{I}}(a) = -\sqrt{\pi a} \frac{2\mu(a, 0)}{1+\kappa} \sum_{n=1}^{N} B_n$$
$$K_{\mathrm{II}}(a) = -\sqrt{\pi a} \frac{2\mu(a, 0)}{1+\kappa} \sum_{n=1}^{N} A_n \tag{38}$$

and the SIFs at the crack tip $x = -a$ are

$$K_{\mathrm{I}}(-a) = \sqrt{\pi a} \frac{2\mu(-a, 0)}{1+\kappa} \sum_{n=1}^{N} (-1)^n B_n$$
$$K_{\mathrm{II}}(-a) = \sqrt{\pi a} \frac{2\mu(-a, 0)}{1+\kappa} \sum_{n=1}^{N} (-1)^n A_n \tag{39}$$

Table 2 shows the SIFs (normalized by $\sigma_0\sqrt{\pi a}$) for various values of $a\delta$ (nonhomogeneity parameter) and two crack orientations, $\theta = 0$ and $\theta = \pi/2$, under uniform crack surface pressure σ_0. The angle $\theta = 0$ corresponds to a crack aligned with the material gradation direction. The problem becomes symmetric about the crack line and thus $K_{\mathrm{II}} = 0$. When $\theta = \pi/2$, the crack is perpendicular to the material gradation direction and the problem is symmetric about $x = 0$; hence, $K_{\mathrm{I}}(-a) = K_{\mathrm{I}}(a)$ and $K_{\mathrm{II}}(-a) = -K_{\mathrm{II}}(a)$. Table 3 shows the normalized SIFs for various values of $a\delta$ and various crack orientations under uniform crack surface pressure σ_0. These results warrant careful examination in applications for defect assessment. For example, one surprising result shown in Table 3 is that the maximum values of K_{I} and K_{II} do not generally correspond to the limiting crack orientations $\theta = 0$ and $\theta = \pi/2$. Also, the values of θ corresponding to the maximum SIFs depend on the nonhomogeneity parameter $a\delta$. More detailed SIF results for a single crack under various loading conditions can be found in Konda and Erdogan (1994).

2.13.3.2.2 Thermal loads

Thermal loads often have a pronounced role in industrial applications of FGMs. The theoretical treatment of cracks under thermal

Table 2 Normalized SIFs under uniform crack surface pressure.

	$a\delta$				
Normalized SIFs	*0.1*	*0.25*	*0.5*	*1.0*	*2.5*
$\theta = 0$ $K_{\mathrm{I}}(a)$	1.023	1.055	1.103	1.189	1.382
$K_{\mathrm{I}}(-a)$	0.975	0.936	0.871	0.757	0.536
$\theta = \pi/2$ $K_{\mathrm{I}}(a)$	1.008	1.036	1.101	1.258	1.808
$K_{\mathrm{II}}(a)$	0.026	0.065	0.129	0.263	0.697

After Konda and Erdogan (1994).

Table 3 Effects of the nonhomogeneity parameter $a\delta$ and the crack orientation θ on the normalized SIFs under uniform crack surface pressure.

	θ/π					
Normalized SIFs	*0.0*	*0.1*	*0.2*	*0.3*	*0.4*	*0.5*
$a\delta = 0.1$ $K_I(a)$	1.023	1.023	1.022	1.020	1.015	1.008
$K_I(-a)$	0.975	0.977	0.983	0.991	1.003	1.008
$K_{II}(a)$	0.000	0.010	0.019	0.024	0.027	0.026
$-K_{II}(-a)$	0.000	0.006	0.012	0.018	0.023	0.026
$a\delta = 0.25$ $K_I(a)$	1.055	1.057	1.061	1.061	1.053	1.036
$K_I(-a)$	0.936	0.943	0.962	0.987	1.014	1.036
$K_{II}(a)$	0.000	0.030	0.054	0.067	0.070	0.065
$-K_{II}(-a)$	0.000	0.011	0.024	0.039	0.054	0.065
$a\delta = 0.5$ $K_I(a)$	1.103	1.113	1.133	1.145	1.135	1.101
$K_I(-a)$	0.871	0.887	0.931	0.990	1.050	1.101
$K_{II}(a)$	0.000	0.073	0.126	0.149	0.148	0.129
$-K_{II}(-a)$	0.000	0.013	0.034	0.064	0.099	0.129
$a\delta = 1.0$ $K_I(a)$	1.189	1.222	1.294	1.348	1.336	1.258
$K_I(-a)$	0.757	0.788	0.878	1.004	0.139	1.258
$K_{II}(a)$	0.000	0.179	0.306	0.352	0.327	0.263
$-K_{II}(-a)$	0.000	0.010	0.039	0.099	0.181	0.263

After Konda and Erdogan (1994)

loads is similar to that for cracks under mechanical loads. Under steady-state thermal loading conditions, Noda and Jin (1993) studied a crack parallel to the boundaries of an infinite strip. Jin and Noda (1994b) considered an edge crack in a nonhomogeneous half plane. Erdogan and Wu (1996) investigated a crack perpendicular to the boundaries of an infinite strip. Nemat-Alla and Noda (2000) considered an edge crack problem in a semi-infinite FGM plate with a bidirectional gradation in the coefficient of thermal expansion. Under transient thermal loading conditions, Jin and Noda (1994c) studied a crack parallel to the boundary of a nonhomogeneous half plane. Jin and Batra (1996b) investigated an edge crack in an FGM strip. Kokini and Case (1997) considered both edge and interface cracks in functionally graded ceramic coatings. Choi *et al.* (1998b) investigated collinear cracks in a layered half plane with a graded homogeneous interfacial zone. Wang *et al.* (2000) developed a multilayered material model to study various crack problems in FGMs under thermal loads. For a comprehensive review on thermal stresses in FGMs and related topics, see the review paper by Noda (1999).

By using a multilayered material model, Jin and Paulino (2001) studied an edge crack in an elastic homogeneous but thermally nonhomogeneous strip subjected to transient temperature boundary conditions as shown in Figure 5. Here a is the crack length, b is the strip thickness, $N+1$ is the total number of homogeneous layers, and T_0 and T_b are boundary thermal loads. By means of the Laplace transform and an asymptotic analysis, they obtained an analytical first-order temperature solution for short times and calculated thermal stress intensity factors (TSIF) (normalized by $E\alpha_0 T_0\sqrt{\pi b}/(1-\nu)$, where E and ν are Young's modulus and Poisson's ratio, respectively, and α_0 is the thermal expansion coefficient of the first homogeneous layer). Figure 6(a) shows the normalized TSIFs for edge cracks with lengths $a/b = 0.1$, 0.3, and 0.5 in a homogeneous strip

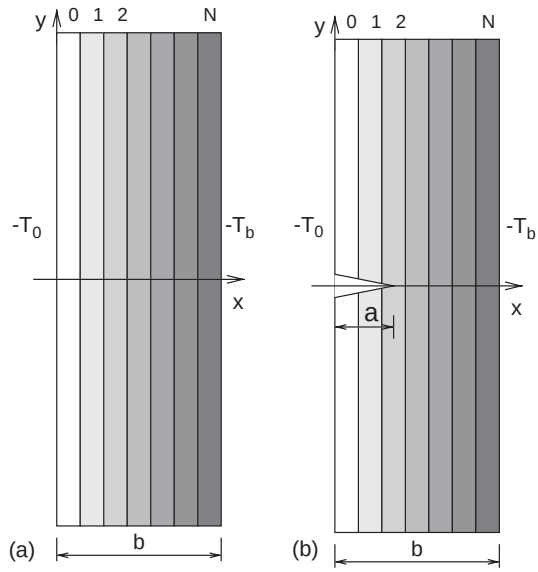

Figure 5 An FGM strip occupying the region $0 \le X \le b$ and $|y| < \infty$. The bounding surfaces of the strip are subjected to uniform thermal loads T_0 and T_b: (a) a layered material and (b) an edge crack in the layered material.

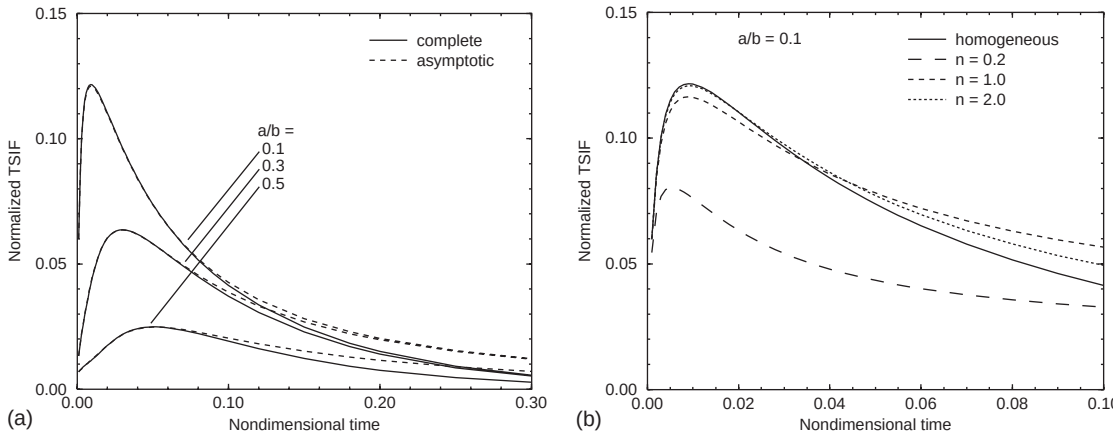

Figure 6 (a) Normalized TSIFs for a homogeneous strip: asymptotic solution versus complete solution and (b) TSIFs for the FGM strip for various material nonhomogeneity parameter n (after Jin and Paulino, 2001).

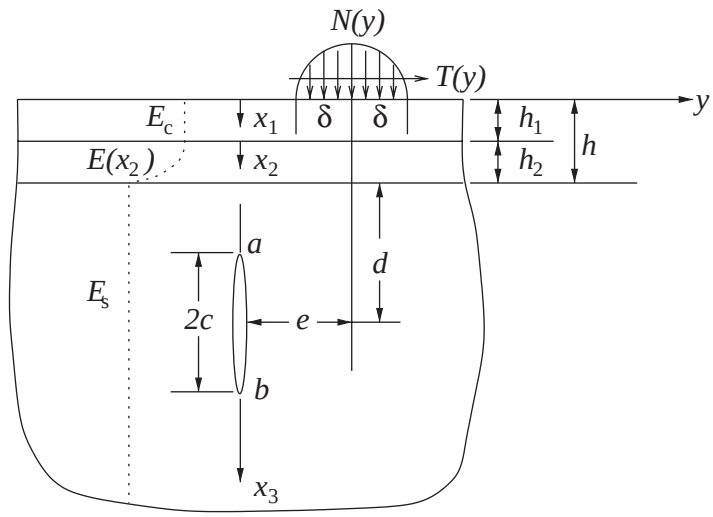

Figure 7 Schematic of a coating/substrate system with an FGM interlayer and a crack under Hertzian contact with friction.

based on the asymptotic solution and the complete solution. The TSIFs based on the asymptotic solution show good agreement with those based on the complete solution for times up to approximately $\tau = 0.1$, where τ is the nondimensional time given by $\tau = t\kappa_0/b^2$ in which t is time and κ_0 is the thermal diffusivity of the first homogeneous layer. Figure 6(b) shows the normalized TSIFs versus nondimensional time τ for cracks in both homogeneous and TiC/SiC FGM strips for the volume fraction profiles $n = 0.2$, 1.0, and 2.0, where n is the power index in the SiC volume fraction function given by (see Figure 2)

$$V_{\mathrm{SiC}}(X) = (X/b)^n \tag{40}$$

The peak TSIFs for the FGM are lower than that for the homogeneous strip.

2.13.3.2.3 Contact loads

The application of FGMs as wear-resistant coatings introduces contact loads in the fracture analysis. Some crack problems of FGMs subjected to contact loads have been studied by Choi (2001b) and Dag and Erdogan (2002).

Choi (2001b) studied a crack in a semi-infinite homogeneous substrate coated by a two-layer material system with an FGM interlayer and a homogeneous top layer, as shown in Figure 7. The top and the FGM layers have thicknesses of h_1 and h_2, respectively. The substrate contains a crack of length $2c$ which is perpendicular to the coating surface and d is the distance between the center of the crack and the interface of the substrate with the FGM layer. The surface of the top layer is loaded by a moving contact pressure with friction, which can be approximately described

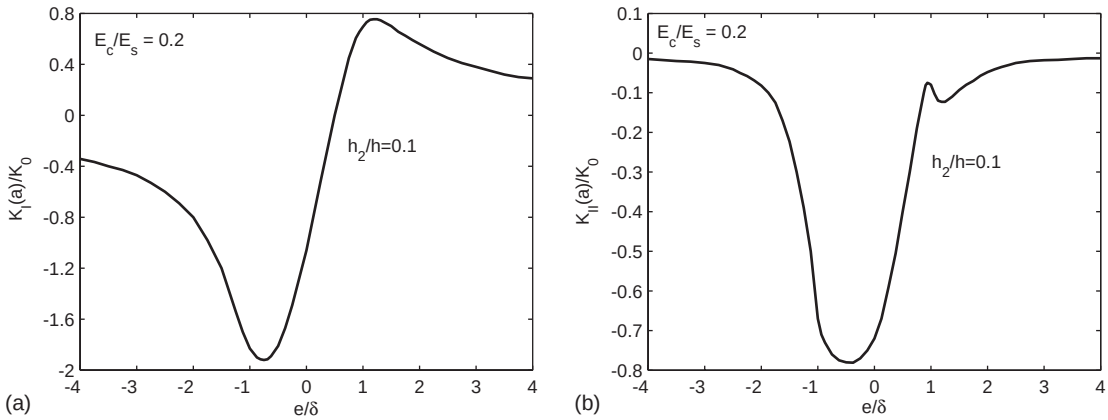

Figure 8 Mixed-mode SIFs for $E_c/E_s = 0.2$, $d/c = h/c = 1.0$, $\delta/c = 5.0$, and $f = 0.7$: (a) normalized mode I SIF at crack tip $x_3 = a$ and (b) normalized mode II SIF at crack-tip $x_3 = a$. See Figure 7 to identify the crack-tip location (after Choi, 2001b).

by the Hertzian contact load

$$N(y) = p_0\sqrt{1 - \left(\frac{y-e}{\delta}\right)^2} \qquad T(y) = fN(y), \quad |y-e| < \delta \tag{41}$$

where $N(y)$ is the normal contact pressure, $T(y)$ the tangential traction, p_0 the peak pressure, δ the contact half-width, e the distance between the contact center and the crack, and f the friction coefficient. The Poisson's ratio is assumed constant throughout the medium and Young's modulus is

$$E = E_c, \quad 0 \le x_1 \le h_1 \tag{42}$$

$$E = E_c \exp(\beta x_2), \quad 0 \le x_2 \le h_2 \tag{43}$$

$$E = E_s, \quad 0 \le x_3 \le \infty \tag{44}$$

where x_i $(i = 1, 2, 3)$ is the local x-coordinate in each layer. By using a singular integral equation approach, Choi (2001b) solved the crack problem of Figure 7 and studied effects of the material nonhomogeneity and contact parameters on SIFs. Figure 8 shows the SIFs (normalized by $K_0 = p_0\sqrt{c}$) for $E_c/E_s = 0.2$, $d/c = h/c = 1.0$, $\delta/c = 5.0$, and $f = 0.7$. The thickness ratio is chosen as $h_2/h = 0.1$.

When the contact moves from the left side of the crack $(e/\delta < 0)$ toward the crack $(e/\delta < 0)$, the absolute value of the mode I SIF, K_I increases first, reaches a maximum, and then decreases. K_I remains negative for $e/\delta \le 0$. The absolute mode II SIF, K_{II}, follows a similar pattern. When the contact moves from the crack to its right side $(e/\delta > 0)$, K_I increases and becomes positive near $e/\delta = 0.5$ or greater, depending on the friction coefficient f. At the same time, K_{II} remains negative but $|K_{II}|$ decreases and reaches a peak near $e/\delta = 1.0$. When $f = 0$, i.e., frictionless contact, K_I is symmetric about the crack line and is negative for all contact locations, while K_{II} is antisymmetric. The negative K_I values in Figure 8(a) simply indicate crack closure at those locations, and are shown just to illustrate this effect. The absolute values of K_I and K_{II} increase with increasing f when $e/\delta < 0$. When $e/\delta > 0$, the maximum values of positive K_I and K_{II} increase with increasing f. As to the effect of material nonhomogeneity on the SIFs, a general observation by Choi (2001b) is that increasing the thickness of the FGM layer causes some increase in the magnitude of the SIFs, especially for K_I. A thinner FGM interlayer, to some extent, becomes more effective in shielding the crack tip.

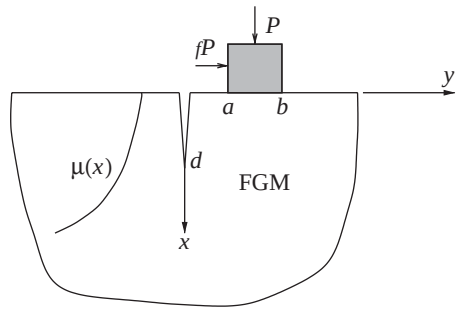

Figure 9 A surface crack in a semi-infinite FGM medium under a sliding stamp.

Dag and Erdogan (2002) investigated a surface crack in a nonhomogeneous half plane loaded by a sliding rigid stamp. Figure 9 shows the contact crack problem, where P is the contact load, f is the friction coefficient, d is the crack length, and a and b are the y-coordinates of the left and right ends of the stamp,

respectively. The shear modulus and the Poisson ratio of the graded medium are assumed as

$$\mu = \mu_0 \exp(\gamma x), \quad \nu = \text{const.} \tag{45}$$

Dag and Erdogan (2002) also used a singular integral equation approach to solve the contact crack problem of Figure 9 and calculated SIFs versus a/d for various values of the material nonhomogeneous parameter γd and friction coefficient f. Detailed results and discussions can be found in Dag and Erdogan (2002).

2.13.3.3 Crack Growth

Crack extension in FGMs may follow one of two scenarios. In the first case, the crack lies in the direction perpendicular to the material gradation. Clearly, the crack growth mode is mixed and the crack deflects from the original orientation. In the second case, the crack propagation occurs in the material gradation direction under mode I loading conditions. This section first discusses the crack deflection problem, i.e., the determination of crack propagation direction. The section concludes with an initial discussion of fracture toughness under stable extension (R-curve).

2.13.3.3.1 Crack deflection

SIFs at a kinked crack tip determine the crack deflection direction at the load when the crack starts to propagate. Several crack-kinking theories exist to predict the kink direction, e.g., the maximum energy release rate criterion, the maximum circumferential stress theory, and so on. The maximum energy release rate criterion states that the crack growth occurs along the direction which provides the maximum energy release rate. The maximum circumferential stress theory assumes that the crack propagation direction corresponds to the one at which the circumferential stress reaches the maximum. The maximum circumferential stress theory is often used for the study of crack growth direction in FGMs. According to this theory, the crack deflection angle relative to the original crack (tangent) line, ϕ, is

$$K_{\mathrm{I}} \sin\phi - K_{\mathrm{II}}(3\cos\phi - 1) = 0 \tag{46}$$

In general, numerical methods are used to calculate the SIFs at the tip of a finite kinked crack (Becker *et al.*, 2001). For small-kink cracks, however, the SIFs at the kinked crack tip may be calculated based on the SIFs for the main crack tip. Gu and Asaro (1997b) presented a crack deflection model for small-kink conditions. The model postulates the idea of a local homogeneous core near the main crack tip characterized by the near-tip fields, Equations (22) and (23). In this core region, Young's modulus and the Poisson ratio are E_{tip} and ν_{tip}, respectively, as shown in Figure 10. Under those assumptions, the small crack kinking model presented by Cotterell and Rice (1980) may be applied to FGMs. Cotterell and Rice (1980) assumed that the SIFs at the kinked crack tip could be expressed as (see also Karihaloo, 1982)

$$\begin{aligned} K_{\mathrm{I}}^{*} &= C_{11}(\phi)K_{\mathrm{I}} + C_{12}(\phi)K_{\mathrm{II}} \\ K_{\mathrm{II}}^{*} &= C_{21}(\phi)K_{\mathrm{I}} + C_{22}(\phi)K_{\mathrm{II}} \end{aligned} \tag{47}$$

where K_{I}^{*} and K_{II}^{*} are the SIFs at the kinked crack tip, K_{I} and K_{II} are the SIFs at the main crack tip, ϕ is the kink angle (see Figure 10), and $C_{ij}\,(i, j = 1, 2)$ are coefficients depending on ϕ. For small kink angle, using the first order approximation, Cotterell and Rice (1980) obtained

$$\begin{aligned} C_{11} &= \frac{1}{4}\left(3\cos\frac{\phi}{2} + \cos\frac{3\phi}{2}\right) \\ C_{12} &= -\frac{3}{4}\left(\sin\frac{\phi}{2} + \sin\frac{3\phi}{2}\right) \\ C_{21} &= \frac{1}{4}\left(\sin\frac{\phi}{2} + \sin\frac{3\phi}{2}\right) \\ C_{22} &= \frac{1}{4}\left(\cos\frac{\phi}{2} + \cos\frac{3\phi}{2}\right) \end{aligned} \tag{48}$$

They showed that, for homogeneous materials, SIFs calculated using Equations (47) and (48) are in good agreement with exact solutions for ϕ up to 40° (the error is less than 5%).

With the SIFs at the kinked crack tip given by Equation (47), the crack growth direction can be obtained by fracture criteria such as the

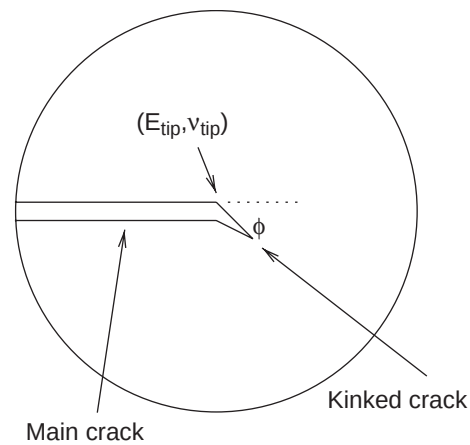

Figure 10 Crack-tip kinking.

maximum energy release rate criterion or the maximum circumferential stress criterion. Gu and Asaro (1997b) calculated the crack growth angles for a double cantilever beam and a four-point bending specimen by using the above model. The material properties were assumed to vary exponentially in the specimen width direction. They observed a strong effect of material gradient on the kink angle when the crack tip is at the middle of the FGM, but the effect becomes small when the crack tip lies near the boundaries of the FGM.

2.13.3.3.2 Fracture toughness and the R-curve

For FGMs, the fracture toughness generally varies with spatial position. For example, a strong fracture toughness gradation exists in ceramic/metal FGMs because the toughness of the metal greatly exceeds that of the ceramic. A very simple approach to determine the fracture toughness of ceramic/metal FGMs adopts a rule of mixtures. For example, Jin and Batra (1996a) assumed that the critical energy release rate for the FGM, $G_{IC}(X)$, may be expressed as follows:

$$G_{IC}(X) = V_{met}(X)G_{IC}^{met} + [1 - V_{met}(X)]G_{IC}^{cer} \quad (49)$$

where G_{IC}^{met} and G_{IC}^{cer} are the critical energy release rates of the metal and ceramic, respectively, V_{met} (X) is the metal volume fraction, and X is the material gradation direction. Note that

$$\begin{aligned} G_{IC}(X) &= \frac{1 - \nu^2(X)}{E(X)} K_{IC}^2 \\ G_{IC}^{met} &= \frac{1 - \nu_{met}^2}{E_{met}} (K_{IC}^{met})^2 \\ G_{IC}^{cer} &= \frac{1 - \nu_{cer}^2}{E_{cer}} (K_{IC}^{cer})^2 \end{aligned} \quad (50)$$

where $K_{IC}(X)$, K_{IC}^{met}, and K_{IC}^{cer} are the fracture toughnesses of the FGM, metal and ceramic, respectively, $E(X)$, E_{met}, and E_{cer} are Young's moduli of the FGM, metal and ceramic, respectively, and $\nu(X)$, ν_{met}, and ν_{cer} are the Poisson ratios of the FGM, metal and ceramic, respectively. The fracture toughness of the FGM is then obtained as follows (Jin and Batra, 1996a):

$$K_{IC}(X) = \left\{ \frac{E(X)}{1 - \nu^2(X)} \left[\frac{(1 - \nu_{met}^2) V_{met}(X)}{E_{met}} (K_{IC}^{met})^2 + \frac{(1 - \nu_{cer}^2)(1 - V_{met}(X))}{E_{cer}} (K_{IC}^{cer})^2 \right] \right\}^{1/2} \quad (51)$$

The above equation indicates that the fracture toughness of the FGM varies with X. When the crack grows from the ceramic-rich region into the metal-rich region, the toughness of the FGM increases significantly since the fracture toughness of the metal greatly exceeds that of the ceramic. However, Equation (51) probably overestimates the fracture toughness of the FGM given the imperfections that exist between the ceramic and metal particles in a ceramic/metal FGM which are not considered in such a simple mixture relationship. To improve the rule of mixture estimates of fracture toughness for FGMs, Jin and Batra (1996a, 1998) proposed a crack-bridging model. In the crack-bridging model, a bridging zone exists ahead of the original main crack with the following constitutive law that relates the bridging traction, σ, to the relative opening displacement of the bridging surfaces

$$\sigma = \sigma_0 (1 - \delta/\delta_0)^n \quad (52)$$

where σ_0 is the maximum bridging traction, δ_0 is a critical opening displacement at which the bridging traction vanishes, and n is a softening index. By using both the rule of mixture estimate and the crack-bridging model, Jin and Batra (1996a) calculated the fracture toughness and R-curve for an edge cracked infinite strip made of an Al_2O_3/Ni FGM. Their result shows that the fracture toughness significantly increases when the crack grows from the ceramic-rich region towards the metal-rich region. The rule of mixture estimate of the fracture toughness exceeds that predicted from the crack-bridging model. Cai and Bao (1998) also studied crack growth in a ceramic/metal graded coating using a more simplified bridging model with constant bridging traction. However, the simple crack-bridging models may not be applicable to the ceramic–metal interconnected region (percolation region) in an FGM (see midportion of Figure 1). A phenomenological cohesive model, proposed by Jin *et al.* (2002), may be used for the whole range of an FGM component—see discussion in Section 2.13.4.3.

2.13.3.4 Dynamic Fracture

2.13.3.4.1 Crack-tip fields for a propagating crack

Parameswaran and Shukla (1999) have studied crack-tip stress and deformation fields for cracks propagating in FGMs with either a linearly varying or an exponentially varying shear modulus. In the case of a linearly varying modulus, the mass density remains constant, while in the case of an exponentially varying modulus, the mass density follows the

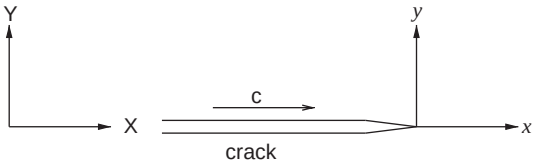

Figure 11 A propagating crack with constant velocity c.

same exponential function. While such assumptions do not reflect real engineering materials, they enable analytical solutions and thus allow one to gain insight into the nature of the dynamic crack-tip fields. This section begins with an introduction of those crack-tip field results.

(i) Crack-tip fields for linear variation of shear modulus and constant mass density

Consider a semi-infinite crack propagating at a constant velocity c in the positive X-direction in an FGM as shown in Figure 11. The shear modulus of the FGM follows the form

$$\mu = \mu_0(1 + \alpha X) \tag{53}$$

where μ_0 and α are material constants. The Poisson ratio (ν) and the mass density (ρ) remain constant. The Lame constant λ is then given by

$$\lambda = \lambda_0(1 + \alpha X) \tag{54}$$

where λ_0 is a constant. Under these assumptions, the governing equations of the dynamic problem under plane-strain conditions are the equations of motion

$$\frac{\partial \sigma_{XX}}{\partial X} + \frac{\partial \sigma_{XY}}{\partial Y} = \rho \frac{\partial^2 u}{\partial t^2}, \quad \frac{\partial \sigma_{XY}}{\partial X} + \frac{\partial \sigma_{YY}}{\partial Y} = \rho \frac{\partial^2 v}{\partial t^2} \tag{55}$$

the strain–displacement relations

$$\varepsilon_{XX} = \frac{\partial u}{\partial X}, \quad \varepsilon_{YY} = \frac{\partial v}{\partial Y}, \quad \varepsilon_{XY} = \frac{1}{2}\left(\frac{\partial u}{\partial Y} + \frac{\partial v}{\partial X}\right) \tag{56}$$

and Hooke's law

$$\begin{aligned} \sigma_{XX} &= (1 + \alpha X)[(\lambda_0 + 2\mu_0)\varepsilon_{XX} + \lambda_0 \varepsilon_{YY}] \\ \sigma_{XX} &= (1 + \alpha X)[(\lambda_0 + 2\mu_0)\varepsilon_{XX} + \lambda_0 \varepsilon_{YY}] \\ \sigma_{XY} &= 2(1 + \alpha X)\mu_0 \varepsilon_{XY} \end{aligned} \tag{57}$$

We introduce the dilatation (Δ) and rotation (ω) by

$$\Delta = \frac{\partial u}{\partial X} + \frac{\partial v}{\partial Y}, \quad \omega = \frac{\partial v}{\partial X} - \frac{\partial u}{\partial Y} \tag{58}$$

The equations of motion can then be expressed by Δ and ω as follows:

$$\begin{aligned} &\mu_0(1 + \alpha X)\nabla^2 \Delta + 2\mu_0 \alpha \frac{\partial \Delta}{\partial X} - \frac{2\mu_0 \alpha}{\lambda_0/\mu_0 + 2}\frac{\partial \omega}{\partial Y} \\ &\quad = \frac{\rho}{\lambda_0/\mu_0 + 2}\frac{\partial^2 \Delta}{\partial t^2} \\ &\mu_0(1 + \alpha X)\nabla^2 \omega + 2\mu_0 \alpha \frac{\partial \omega}{\partial X} + 2\lambda_0 \alpha \frac{\partial \Delta}{\partial Y} = \rho \frac{\partial^2 \omega}{\partial t^2} \end{aligned} \tag{59}$$

The above equations reduce to the corresponding wave equations of dilatation and rotation for homogeneous materials by setting α equal to zero. However, due to the nonhomogeneous nature of the material, the equations remain coupled in the two fields Δ and ω, through the nonhomogeneity parameter α. When Equations (59) are written in a moving rectangular coordinate system (x, y) centered at the crack tip as shown in Figure 11, we have

$$\begin{aligned} &\alpha_1^2 \frac{\partial^2 \Delta}{\partial x^2} + \frac{\partial^2 \Delta}{\partial y^2} + \beta x \nabla^2 \Delta + 2\beta \frac{\partial \Delta}{\partial x} - \frac{2\beta}{\lambda_0/\mu_0 + 2}\frac{\partial \omega}{\partial y} = 0 \\ &\alpha_2^2 \frac{\partial^2 \omega}{\partial x^2} + \frac{\partial^2 \omega}{\partial y^2} + \beta x \nabla^2 \omega + 2\beta \frac{\partial \omega}{\partial x} + 2\beta \frac{\partial \delta}{\partial y} = 0 \end{aligned} \tag{60}$$

where

$$\begin{aligned} \alpha_1 &= \left[1 - \frac{\rho c^2}{\mu_{\text{tip}}(\lambda_0/\mu_0 + 2)}\right]^{1/2} \\ \alpha_2 &= \left[1 - \frac{\rho c^2}{\mu_{\text{tip}}}\right]^{1/2} \\ \beta &= \mu_0 \alpha / \mu_{\text{tip}} \end{aligned} \tag{61}$$

in which μ_{tip} is the shear modulus at the crack tip.

By using an asymptotic analysis, Parameswaran and Shukla (1999) obtained the crack-tip solutions for Δ and ω, and found that the crack-tip stress and velocity fields have the following form:

$$\sigma_{\alpha\beta} = \frac{1}{\sqrt{2\pi r}}\{K_{\text{I}}(t)\tilde{\Sigma}_{\alpha\beta}^{(1)}(\theta, c) + K_{\text{II}}(t)\tilde{\Sigma}_{\alpha\beta}^{(2)}(\theta, c)\} \quad r \to 0 \tag{62}$$

$$\dot{u}_\alpha = \frac{c}{\mu_{\text{tip}}\sqrt{2\pi r}}\{K_{\text{I}}(t)\tilde{V}_\alpha^{(1)}(\theta, c) + K_{\text{II}}(t)\tilde{V}_\alpha^{(2)}(\theta, c)\} \quad r \to 0 \tag{63}$$

which are identical to the fields for homogeneous materials. Note that Equations (62) and (63) have a similar form to those reported in Equations (22) and (23) for the quasistatic case, but with displacements replaced by velocities including the time dependence of

SIFs. In the above expressions, $\sigma_{\alpha\beta}$ are stresses, $\dot{u}_\alpha$ are velocities, (r, θ) are the polar coordinates centered at the crack tip, $K_{\mathrm{I}}(t)$ and $K_{\mathrm{II}}(t)$ are mode I and mode II dynamic SIFs, respectively, $\tilde{\Sigma}^{(1)}_{\alpha\beta}(\theta, c)$ and $\tilde{\Sigma}^{(2)}_{\alpha\beta}(\theta, c)$ are standard angular distribution functions of stresses for propagating cracks, and $\tilde{V}^{(1)}_{\alpha}(\theta, c)$ and $\tilde{V}^{(2)}_{\alpha}(\theta, c)$ are standard angular distribution functions of velocities, which can be found in dynamic fracture mechanics books, e.g., Freund (1990). Besides the singular term of the crack-tip asymptotic fields, Parameswaran and Shukla (1999) also obtained higher order terms of the Δ and ω fields with the solutions up to the third order term given by

$$\begin{aligned}\Delta = {} & A_0 r_1^{-1/2}\cos\frac{\theta_1}{2} + A_1 + A_2 r_1^{1/2}\cos\frac{\theta_1}{2} \\ & - \frac{\beta}{2\alpha_1^2}A_0 r_1^{1/2}\cos\frac{3\theta_1}{2} \\ & + \frac{4\beta\alpha_2}{(\alpha_1^2-\alpha_2^2)(\lambda_0/\mu_0+2)}B_0 r_2^{1/2}\cos\frac{\theta_2}{2} \\ & + \frac{3(1-\alpha_1^2)\beta}{16\alpha_1^2}A_0 r_1^{1/2}\left(\frac{1}{6}\cos\frac{7\theta_1}{2} + \cos\frac{3\theta_1}{2}\right) \\ & + C_0 r_1^{-1/2}\sin\frac{\theta_1}{2} + C_2 r_1^{1/2}\sin\frac{\theta_1}{2} \\ & + \frac{\beta}{2\alpha_1^2}C_0 r_1^{1/2}\sin\frac{3\theta_1}{2} \\ & - \frac{4\beta\alpha_2}{(\alpha_1^2-\alpha_2^2)(\lambda_0/\mu_0+2)}D_0 r_2^{1/2}\sin\frac{\theta_2}{2} \\ & - \frac{3(1-\alpha_1^2)\beta}{16\alpha_1^2}C_0 r_1^{1/2}\left(\frac{1}{6}\sin\frac{7\theta_1}{2} + \sin\frac{3\theta_1}{2}\right)\end{aligned} \tag{64}$$

$$\begin{aligned}\omega = {} & -B_0 r_2^{-1/2}\sin\frac{\theta_2}{2} + B_2 r_2^{1/2}\sin\frac{\theta_2}{2} \\ & - \frac{\beta}{2\alpha_2^2}B_0 r_2^{1/2}\sin\frac{3\theta_2}{2} + \frac{4\beta\alpha_1}{(\alpha_2^2-\alpha_1^2)}A_0 r_1^{1/2}\sin\frac{\theta_1}{2} \\ & - \frac{3(1-\alpha_2^2)\beta}{16\alpha_2^2}B_0 r_2^{1/2}\left(\frac{1}{6}\sin\frac{7\theta_2}{2} + \sin\frac{3\theta_2}{2}\right) \\ & + D_0 r_2^{-1/2}\cos\frac{\theta_2}{2} + D_1 + D_2 r_2^{1/2}\cos\frac{\theta_2}{2} \\ & - \frac{\beta}{2\alpha_2^2}D_0 r_2^{1/2}\cos\frac{3\theta_2}{2} - \frac{4\beta\alpha_1}{(\alpha_2^2-\alpha_1^2)}C_0 r_1^{1/2}\cos\frac{\theta_1}{2} \\ & + \frac{3(1-\alpha_2^2)\beta}{16\alpha_2^2}D_0 r_2^{1/2}\left(\frac{1}{6}\cos\frac{7\theta_2}{2} + \cos\frac{3\theta_2}{2}\right)\end{aligned} \tag{65}$$

where

$$r_i = (x^2 + \alpha_i^2 y^2)^{1/2}, \quad \theta_i = \arctan\frac{\alpha_i y}{x}, \quad i = 1, 2 \tag{66}$$

A_0, B_0, C_0, and D_0 are related to the dynamic SIFs by

$$\begin{aligned}A_0 &= \frac{(1+\alpha_2^2)(1-\alpha_1^2)}{4\alpha_1\alpha_2 - (1+\alpha_2^2)^2}\frac{K_{\mathrm{I}}}{\mu_{\mathrm{tip}}\sqrt{2\pi}} \\ B_0 &= \frac{2\alpha_1(1-\alpha_2^2)}{1+\alpha_2^2(1-\alpha_1^2)}A_0 \\ C_0 &= \frac{2\alpha_2(1-\alpha_1^2)}{4\alpha_1\alpha_2 - (1+\alpha_2^2)^2}\frac{K_{\mathrm{II}}}{\mu_{\mathrm{tip}}\sqrt{2\pi}} \\ D_0 &= -\frac{1+\alpha_2^2(1-\alpha_2^2)}{2\alpha_2(1-\alpha_1^2)}C_0\end{aligned} \tag{67}$$

and A_1, A_2, B_2, C_2, D_1, and D_2 are unknown constants. Note that the first and second-order terms are identical to those for homogeneous materials but the third-order term differs from that for homogeneous materials.

(ii) Crack-tip fields for exponential variation of both shear modulus and mass density

Parameswaran and Shukla (1999) also considered crack-tip fields for a crack propagating in an FGM with the following spatial variation of shear modulus and mass density

$$\mu = \mu_0 \exp(\alpha X), \quad \rho = \rho_0 \exp(\alpha X) \tag{68}$$

where μ_0, ρ_0, and α are material constants. Poisson's ratio (ν) is again assumed constant. Under these assumptions, the equations for the dilatation Δ and rotation ω in the moving rectangular coordinates (x, y) are

$$\begin{aligned}\alpha_1^2\frac{\partial^2\Delta}{\partial x^2} + \frac{\partial^2\Delta}{\partial y^2} + a\frac{\partial\Delta}{\partial x} - \frac{a}{\lambda_0/\mu_0+2}\frac{\partial\omega}{\partial y} = 0 \\ \alpha_2^2\frac{\partial^2\omega}{\partial x^2} + \frac{\partial^2\omega}{\partial y^2} + \alpha\frac{\partial\omega}{\partial x} - a\frac{\lambda_0}{\mu_0}\frac{\partial\delta}{\partial y} = 0\end{aligned} \tag{69}$$

where

$$\alpha_1 = \left[1 - \frac{\rho_0 c^2}{\lambda_0 + 2\mu_0)}\right]^{1/2}, \quad \alpha_2 = \left[1 - \frac{\rho_0 c^2}{\mu_0}\right]^{1/2} \tag{70}$$

The leading terms of the asymptotic crack-tip stress and velocity fields are again found identical to those for homogeneous materials. Parameswaran and Shukla (1999) also obtained the crack-tip Δ and ω solutions up to the third-order term.

2.13.3.4.2 Dynamic SIFs

Due to difficulties of analytical modeling, only limited solutions for dynamic stress intensity factors (DSIFs) are available. Babaei and Lukasiewicz (1998) considered a crack in an FGM layer between two dissimilar half planes under anti-plane shear impact load. Itou (2001) studied DSIFs for a crack in a

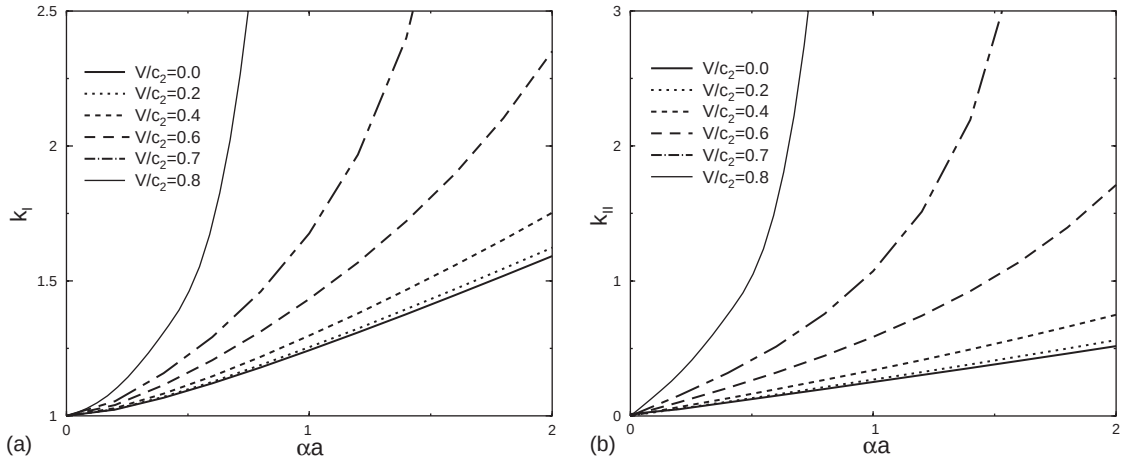

Figure 12 (a) Normalized mode I DSIF versus nonhomogeneity parameter, αa and (b) normalized mode II DSIF versus nonhomogeneity parameter, αa (after Meguid *et al.*, 2002).

nonhomogeneous layer sandwiched between two dissimilar homogeneous materials under in-plane stress wave loading. Li *et al.* (2001) investigated a cylindrical crack in an FGM layer under torsional dynamic loading.

Meguid *et al.* (2002) considered a crack of finite length ($2a$) propagating at a constant velocity c along the x-direction (see Figure 11) in an infinite FGM medium with the following Young's modulus and mass density

$$E = E_0 \exp(\alpha y), \quad \rho = \rho_0 \exp(\alpha y) \tag{71}$$

where E_0, ρ_0, and α are material constants, and Poisson's ratio remains constant. Again, although the above assumptions do not reflect real materials, they are valuable to gain insight into the nature of DSIFs. Under the above assumptions, the Navier–Cauchy equations in the moving coordinates (x, y) become

$$\begin{aligned} &\beta_1 \frac{\partial^2 u}{\partial x^2} + \frac{\partial^2 u}{\partial y^2} + \beta_2 \frac{\partial^2 v}{\partial x \partial y} + \beta\left(\frac{\partial u}{\partial y} + \frac{\partial v}{\partial x}\right) = 0 \\ &\beta_3 \frac{\partial^2 v}{\partial y^2} + \frac{\partial^2 v}{\partial x^2} + \beta_4 \frac{\partial^2 u}{\partial x \partial y} + \beta_3 \beta\left(v \frac{\partial u}{\partial x} + \frac{\partial v}{\partial y}\right) = 0 \end{aligned} \tag{72}$$

where

$$\beta_1 = \frac{2}{1-v}\left(1 - \frac{c^2}{c_1^2}\right), \quad \beta_2 = \frac{1+v}{1-v}$$

$$\beta_3 = \frac{2}{1-v}\left(1 - \frac{c^2}{c_2^2}\right)^{-1}, \quad \beta_4 = \frac{1+v}{1-v}\left(1 - \frac{c^2}{c_2^2}\right)^{-1}$$

$$c_1 = \left[\frac{E_0}{(1-v^2)\rho_0}\right]^{1/2}, \quad c_2 = \left[\frac{E_0}{2(1+v)\rho_0}\right]^{1/2} \tag{73}$$

Meguid *et al.* (2002) solved these governing equations under both normal crack face load, σ_0, and shear load, τ_0, by using an integral equation method. Figure 12(a) shows the mode I DSIF (normalized by $\sigma_0\sqrt{\pi a}$), k_I, versus the nonhomogeneous parameter αa for different crack propagation speeds. k_I increases with increasing αa; and with increasing crack propagation speed, the effect of α increases. Figure 12(b) shows the normalized mode II DSIF, k_{II}, versus the nonhomogeneity parameter αa for different crack propagation speeds. A significant effect of αa upon k_{II} is observed. More detailed DSIF results can be found in the paper of Meguid *et al.* (2002).

2.13.3.5 Viscoelastic Fracture

To date, FGMs have found primary potential application in high-temperature technologies. In general, materials exhibit creep and stress relaxation behavior at high temperatures. Viscoelasticity offers a basis to study the phenomenological behavior of creep and stress relaxation of polymers and polymer-based FGMs fabricated by, e.g., Parameswaran and Shukla (1998), Lambros *et al.* (1999), and Marur and Tippur (2000b); however, those papers are not concerned with viscoelasticity.

The elastic–viscoelastic correspondence principle (or elastic–viscoelastic analogy) represents one of the most useful tools in viscoelasticity because the Laplace transform of the viscoelastic solution can be directly obtained from the corresponding elastic solution. However, the correspondence principle does not in general hold for FGMs. To avoid this problem, Paulino and Jin (2001a) have shown that the correspondence principle can

still be used to obtain the viscoelastic solution for a class of FGMs exhibiting relaxation or creep functions with separable kernels in space and time. In the development below, the revisited correspondence principle is presented and the solution of a crack problem is given to illustrate application of the correspondence principle to viscoelastic FGMs.

Other studies on crack problems of nonhomogeneous viscoelastic materials directly solve the viscoelastic governing equations. For example, Alex and Schovanec (1996) have considered stationary cracks subjected to antiplane shear loading. Herrmann and Schovanec (1990, 1994) have studied quasistatic and dynamic crack propagation in nonhomogeneous viscoelastic media under antiplane shear conditions. Schovanec and Walton (1987a, 1987b) have also considered quasistatic propagation of a plane-strain mode I crack in a power-law nonhomogeneous linearly viscoelastic body and calculated the corresponding energy release rate. Although these investigations employed a separable form for the relaxation functions, they did not make use of the correspondence principle. When applicable, use of the correspondence principle substantially simplifies solution of viscoelastic problems (see Paulino and Jin, 2001a; 2001b).

2.13.3.5.1 Basic equations

The basic equations of quasi-static viscoelasticity of FGMs are

$$\sigma_{ij,j} = 0, \quad \text{(equilibrium equation)} \tag{74}$$

$$\varepsilon_{ij} = (u_{i,j} + u_{j,i})/2, \quad \text{(strain}-\text{displacement relation)} \tag{75}$$

$$\left.\begin{aligned} s_{ij} &= 2\int_0^t \mu(\boldsymbol{x}, t-\tau)\frac{\mathrm{d}e_{ij}}{\mathrm{d}\tau}\mathrm{d}\tau \\ \sigma_{kk} &= 3\int_0^t K(\boldsymbol{x}, t-\tau)\frac{\mathrm{d}\varepsilon_{kk}}{\mathrm{d}\tau}\mathrm{d}\tau \end{aligned}\right\} \quad \text{(constitutive law)} \tag{76}$$

$$s_{ij} = \sigma_{ij} - \sigma_{kk}\delta_{ij}/3, \quad e_{ij} = \varepsilon_{ij} - \varepsilon_{kk}\delta_{ij}/3 \tag{77}$$

in which σ_{ij} are stresses, ε_{ij} are strains, s_{ij} and e_{ij} are deviatoric components of stress and strain tensors, u_i are displacements, δ_{ij} is the Kronecker delta, $\boldsymbol{x} = (x_1, x_2, x_3)$, $\mu(\boldsymbol{x}, t)$, and $K(\boldsymbol{x}, t)$ are the appropriate relaxation functions, t is the time, the Latin indices have the range 1, 2, 3, and repeated indices imply the summation convention. Note that the relaxation functions also depend on spatial positions, whereas in homogeneous viscoelasticity, they are only functions of time, i.e., $\mu \equiv \mu(t)$ and $K \equiv K(t)$ (Christensen, 1971).

The boundary conditions are given by

$$\sigma_{ij}n_j = S_i, \quad \text{on } B_\sigma \tag{78}$$

$$u_i = \Delta_i, \quad \text{on } B_u \tag{79}$$

where n_j are the components of the unit outward normal to the boundary of the body, S_i are the tractions prescribed on B_σ, and Δ_i are the prescribed displacements on B_u. Notice that B_σ and B_u are required to remain constant with time.

2.13.3.5.2 Correspondence principle, revisited

In general, the standard correspondence principle of homogeneous viscoelasticity does not hold for FGMs. To circumvent this problem, consider a special class of FGMs in which the relaxation functions have the following general form (separable in space and time):

$$\begin{aligned} \mu(\boldsymbol{x}, t) &= \mu_0\tilde{\mu}(\boldsymbol{x})f(t) \\ K(\boldsymbol{x}, t) &= K_0\tilde{K}(\boldsymbol{x})g(t) \end{aligned} \tag{80}$$

The constitutive law Equation (76) then reduces to

$$\begin{aligned} s_{ij} &= 2\mu_0\tilde{\mu}(\boldsymbol{x})\int_0^t f(t-\tau)\frac{\mathrm{d}e_{ij}}{\mathrm{d}\tau}\mathrm{d}\tau \\ \sigma_{kk} &= 3K_0\tilde{K}(\boldsymbol{x})\int_0^t g(t-\tau)\frac{\mathrm{d}\varepsilon_{kk}}{\mathrm{d}\tau}\mathrm{d}\tau \end{aligned} \tag{81}$$

By assuming that the material is initially at rest, the Laplace transforms of the basic Equations (74), (75), (81), and the boundary conditions Equations (78) and (79) are obtained as

$$\bar{\sigma}_{ij,j} = 0 \tag{82}$$

$$\bar{\varepsilon}_{ij} = (\bar{u}_{i,j} + \bar{u}_{j,i})/2 \tag{83}$$

$$\bar{s}_{ij} = 2\mu_0\tilde{\mu}(\boldsymbol{x})p\bar{f}(p)\bar{e}_{ij}, \quad \bar{\sigma}_{kk} = 3K_0\tilde{K}(\boldsymbol{x})p\bar{g}(p)\bar{\varepsilon}_{kk} \tag{84}$$

$$\bar{\sigma}_{ij}n_j = \bar{S}_i, \quad \text{on } B_\sigma \tag{85}$$

$$\bar{u}_i = \bar{\Delta}_i, \quad \text{on } B_u \tag{86}$$

where a bar over a variable represents its Laplace transform, and p is the transform variable. The set of Equations (82)–(84), and conditions Equations (85) and (86) have a form identical to those of nonhomogeneous elasticity with shear modulus $\mu = \mu_0\tilde{\mu}(\boldsymbol{x})$ and bulk modulus $K = K_0\tilde{K}(\boldsymbol{x})$ provided that the transformed viscoelastic variables are associated with the corresponding elastic variables, and $\mu_0 p\bar{f}(p)$ and $K_0 p\bar{g}(p)$ are associated with μ_0 and K_0, respectively. Therefore, the *correspondence principle* of homogeneous viscoelasticity

still holds for the FGM with the material properties given in Equation (80), i.e., the Laplace transformed nonhomogeneous viscoelastic solution can be obtained directly from the solution of the corresponding nonhomogeneous elastic problem by replacing μ_0 and K_0 with $\mu_0 p\bar{f}(p)$ and $K_0 p\bar{g}(p)$, respectively. The final solution is realized upon inverting the transformed solution.

2.13.3.5.3 Viscoelastic models

Among the various models for graded viscoelastic materials, we introduce the *standard linear solid* defined by

$$\mu(\mathbf{x},t) = \mu_\infty(\boldsymbol{x}) + [\mu_e(\boldsymbol{x}) - \mu_\infty(\boldsymbol{x})]\exp[-t/t_\mu(\boldsymbol{x})]$$

$$K(\boldsymbol{x},t) = K_\infty(\boldsymbol{x}) + [K_e(\boldsymbol{x}) - K_\infty(\boldsymbol{x})]\exp[-t/t_K(\boldsymbol{x})] \tag{87}$$

the *power-law model* given by

$$\begin{aligned}\mu(\boldsymbol{x},t) &= \mu_e(\boldsymbol{x})[t_\mu(\boldsymbol{x})/t]^q, \quad K(\boldsymbol{x},t)\\ &= K_e(\boldsymbol{x})[t_K(\boldsymbol{x})/t]^q, \quad 0<q<1\end{aligned} \tag{88}$$

and the *Maxwell material model* expressed by

$$\begin{aligned}\mu(\boldsymbol{x},t) &= \mu_e(\boldsymbol{x})\exp[-t/t_\mu(\boldsymbol{x})],\\ K(\boldsymbol{x},t) &= K_e(\boldsymbol{x})\exp[-t/t_K(\boldsymbol{x})]\end{aligned} \tag{89}$$

where $t_\mu(\boldsymbol{x})$ and $t_K(\boldsymbol{x})$ are the relaxation times in shear and bulk moduli, respectively, and q is a material constant.

The discussion below indicates the revisions needed in the general models so that the correspondence principle holds.

(i) *Standard linear solid* (Equation (87)). If the relaxation times t_μ and t_K are constant, if $\mu_e(\boldsymbol{x})$ and $\mu_\infty(\boldsymbol{x})$ have the same functional form, and if $K_e(\boldsymbol{x})$ and $K_\infty(\boldsymbol{x})$ have the same functional form, then the standard linear solid satisfies assumption Equation (80).

(ii) *Power-law model* (Equation (88)). If the relaxation times t_μ and t_K are independent of spatial position, then the assumption Equation (80) is readily satisfied. Moreover, even if the relaxation times do depend on the spatial position in Equation (88), the correspondence principle may still be applied with some revision, which consists of taking the corresponding nonhomogeneous elastic material with the following properties:

$$\mu = \mu_e(\boldsymbol{x})[t_\mu(\boldsymbol{x})]^q, \quad K = K_e(\boldsymbol{x})[t_K(\boldsymbol{x})]^q \tag{90}$$

instead of $\mu = \mu_e(\boldsymbol{x})$ and $K = K_e(\boldsymbol{x})$.

(iii) *Maxwell material* (Equation (89)). If the relaxation times t_μ and t_K are independent of spatial position, then Equation (80) is satisfied.

2.13.3.5.4 A crack in a viscoelastic FGM strip

Paulino and Jin (2001b, 2001c) have applied the revisited correspondence principle to some antiplane shear crack problems. They also considered (Jin and Paulino, 2002) an infinite nonhomogeneous viscoelastic strip containing a crack of length $2a$, as shown in Figure 13. The FGM strip is subjected to a uniform tension $\sigma_0\Sigma(t)$ in the y-direction along both the lower boundary ($y=-h_1$) and the upper boundary ($y=h_2$), where σ_0 is a constant and $\Sigma(t)$ is a nondimensional function of time t. The crack lies on the x-axis, from $-a$ to a, and the crack surfaces remain traction free.

The extensional relaxation function of the material is given by

$$E = E_0\exp(\beta y/h)f(t) \tag{91}$$

where h is a scale length and $f(t)$ is a nondimensional function of time t, e.g.,

$$f(t) = E_\infty/E_0 + (1 - E_\infty/E_0)\exp(-t/t_0) \quad \text{(linear standard solid)} \tag{92}$$

$$f(t) = (t_0/t)^q \quad \text{(power-law material)} \tag{93}$$

The following form, which is a generalization of the power-law material model is also considered

$$E = E_0\exp(\beta y/h)[t_0\exp(\delta y/h)/t]^q \tag{94}$$

in which the relaxation time depends on y exponentially. In the above expressions, the parameters E_0, E_∞, β, t_0; δ, q are material constants. Poisson's ratio takes on the form (also separable in space and time)

$$\nu = \nu_0(1+\gamma y/h)\exp(\beta y/h)g(t) \tag{95}$$

where ν_0 and γ are material constants, and $g(t)$ is a nondimensional function of time t.

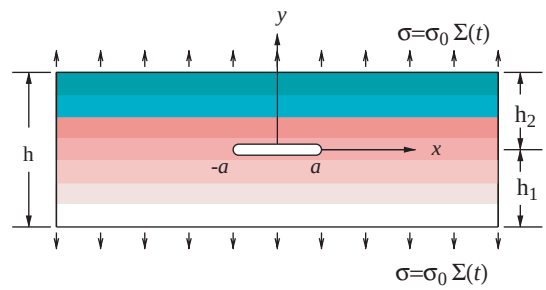

Figure 13 A viscoelastic FGM strip occupies the region $|x|<\infty$ and $-h_1 \le y \le h_2$ with a crack at $|x|\le a$ and $y=0$. The boundaries of the strip ($y=-h_1$, h_2) are subjected to uniform traction $\sigma_0\Sigma(t)$.

It can be clearly seen from Equations (91)–(95) that the relaxation moduli and Poisson's ratio are separable functions in space and time. This is a necessary condition for applying the *revisited correspondence principle* of Paulino and Jin (2001a). This kind of relaxation function may be appropriate for an FGM with its constituent materials having different Young's moduli and Poisson's ratios, but having approximately the same viscoelastic relaxation behavior. Since the FGM is a special composite of its constituents, the viscoelastic relaxation behavior may remain unchanged if its constitutents have the same relaxation behavior. Thus, the relaxation moduli of the FGM would have separable forms in space and time. Further, the material constants β and γ describe the spatial gradation in Young's modulus and the Poisson ratio. Potentially, this kind of FGM may include some polymeric/polymeric materials such as Propylene homopolymer/Acetal copolymer. The relaxation behavior of Propylene homopolymer and Acetal copolymer are found to be similar—see figures 7.5 and 10.3, respectively, of Ogorkiewicz (1970).

According to the correspondence principle, a crack in an elastic strip of an FGM with the following properties,

$$E = E_0 \exp(\beta y/h), \quad \nu = \nu_0(1 + \gamma y/h)\exp(\beta y/h) \tag{96}$$

may be considered. The Laplace transform of the viscoelastic solution is directly obtained from the elastic solution.

Figure 14 shows SIFs, K_{I} and K_{II} (normalized by $\sigma_0\Sigma(t)\sqrt{\pi a}$), versus nondimensional crack length $2a/h$ considering various dimensionless nonhomogeneity parameter β for the linear standard solid and the power-law model with constant relaxation time (see Equations (92) and (93)). The SIFs are identical for both models. The crack is located in the middle of the strip, i.e., $h_2 = 0.5h$. Figure 14(a) shows the results for mode I SIFs. The mode I SIF increases with increasing ratio $2a/h$ for all β values considered here. The SIF is higher than that of the corresponding homogeneous material ($\beta = 0$) and is an even function of β. However, this symmetry remains valid only for the crack located in the center of the strip. Figure 14(b) shows the results for mode II SIFs. The mode II SIF is asymmetric about $\beta = 0$ (again, this antisymmetry is valid only for the crack located in the center of the strip). The absolute value of the mode II SIF increases with increasing $2a/h$. As expected, the mode II SIF is zero for this crack geometry in a homogeneous strip ($\beta = 0$).

Figure 15 shows normalized SIFs versus the nondimensional crack length $2a/h$ for $\beta = 2$ and various values of δ for the power-law material with position-dependent relaxation time (see Equation (94)). The crack is located in the middle of the strip. The effect of spatial position dependence of the relaxation time on the SIFs is reflected through the dimensionless parameter δ (the parameter q is taken as 0.4 in all calculations). Thus the curves for $\delta = \pm 1$ may be obtained from the curve $\delta = 0$ by shifting this curve by $\beta = \mp 0.4$. Figure 15 makes clear that, with respect to the corresponding model for constant relaxation time (i.e., $\delta = 0$), a positive δ increases the SIFs when $\beta > 0$. When $|\beta|$ becomes relatively small compared with $|q\delta|$, the variation of SIFs with δ follows different paths depending on the value of $\beta + q\delta$.

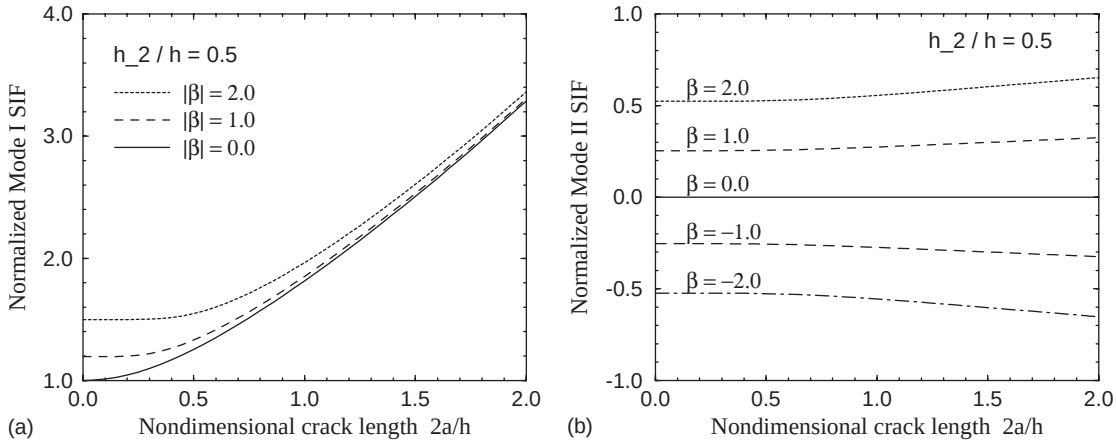

Figure 14 Normalized SIFs versus nondimensional crack length, $2a/h$, for various material nonhomogeneity parameter β considering the linear standard solid and the power-law material with constant relaxation time ($h_2 = 0.5h$): (a) mode I SIF and (b) mode II SIF (after Jin and Paulino, 2002).

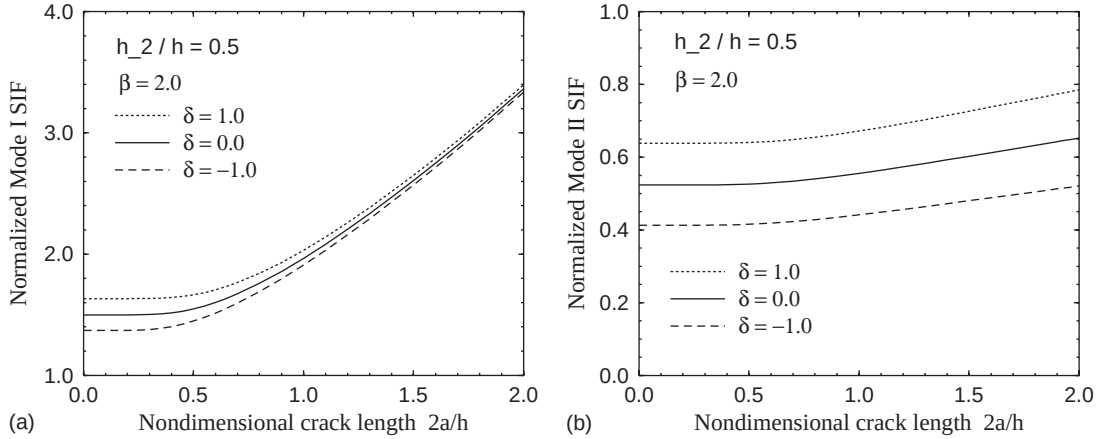

Figure 15 Normalized SIFs versus nondimensional crack length, $2a/h$, for various material nonhomogeneity parameter δ considering the power-law material with position-dependent relaxation time ($\beta = 2.0$, $q = 0.4$, $h_2 = 0.5h$): (a) mode I SIF and (b) mode II SIF (after Jin and Paulino, 2002).

2.13.3.6 J_e-integral

Path independent integrals, especially the J-integral (Eshelby, 1951; Cherepanov, 1967, 1968; Rice, 1968), play an important role in predicting fracture of materials. In general, the J-integral becomes path-dependent for nonhomogeneous materials. Honein and Herrmann (1997) extended the J-integral to certain classes of nonhomogeneous elastic materials with varying Young's modulus in the crack-line direction. For instance, consider a nonhomogeneous material with Poisson's ratio independent of x_1 (crack-line direction) and the shear modulus varying exponentially in the x_1 direction

$$\mu(x_1, x_2) = \mu_0(x_2)\exp(\beta x_1) \tag{97}$$

where $\mu_0(x_2)$ is an arbitrary function of x_2 and β is a material constant. The path-independent integral for this nonhomogeneous material is (Honein and Herrmann, 1997)

$$J_e = \int_\Gamma \left[\left(Wn_1 - \sigma_{ij} n_j \frac{\partial u_i}{\partial x_1} \right) - \frac{\beta}{2} \sigma_{ij} n_j u_i \right] \mathrm{d}s \tag{98}$$

where Γ is a contour enclosing the crack tip, n_1 is the first component of the unit outward normal to Γ, $\sigma_{ij}n_j = S_i$ are the components of tractions along Γ, $\mathrm{d}s$ is an infinitesimal length element along the contour Γ, and W is the strain energy density. The extra term in Equation (98), which appears outside the inner parentheses, arises from the material nonhomogeneity. This extra term maintains the path independence of the J_e-integral for the nonhomogeneous material, Equation (97).

Next consider a nonhomogeneous material with constant Poisson ratio and the following shear modulus

$$\mu(x_1) = \mu_0(\beta x_1 + 1)^\alpha \tag{99}$$

where β and α are material constants. The path-independent integral, derived by Honein and Herrmann (1997), for this nonhomogeneous material is

$$J_e = \int_\Gamma \left[Wn_1 - \sigma_{ij} n_j \frac{\partial u_i}{\partial x_1} + \beta \left(Wx_j n_j - \sigma_{ij} n_j x_k \frac{\partial u_i}{\partial x_k} - \frac{\alpha}{2} \sigma_{ij} n_j u_i \right) \right] \mathrm{d}s \tag{100}$$

Again, note the extra term within parentheses is due to the material nonhomogeneity. Finally, Honein and Herrmann (1997) showed that the J_e-integral is related to SIFs by

$$J_e = \frac{1}{E'_{\mathrm{tip}}} (K_{\mathrm{I}}^2 + K_{\mathrm{II}}^2) \tag{101}$$

where $E'_{\mathrm{tip}} = E_{\mathrm{tip}}$ for plane stress and $E'_{\mathrm{tip}} = E_{\mathrm{tip}}/(1 - \nu_{\mathrm{tip}}^2)$ for plane strain.

2.13.4 FINITE ELEMENT MODELING

2.13.4.1 Graded Finite Elements

The standard parametric finite element (FE) formulation interpolates displacements and coordinates from the element nodal values. Similarly, material properties can also be interpolated from the element nodal values using shape functions. The general approach is

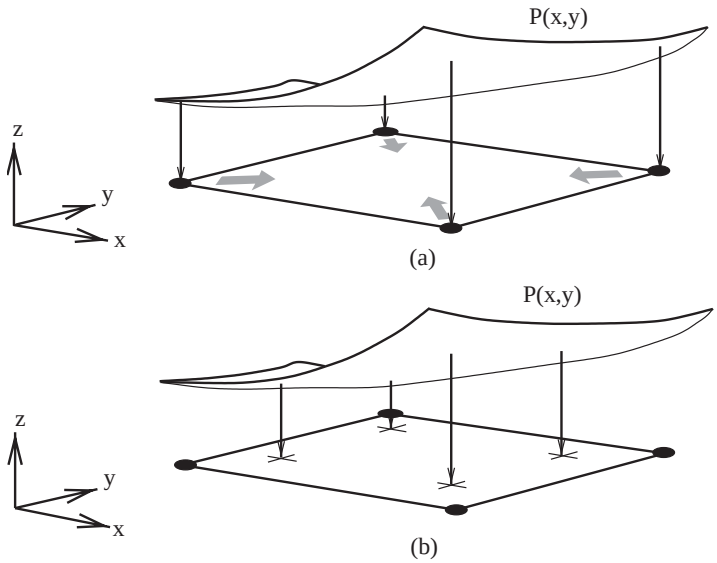

Figure 16 Graded element: (a) generalized isoparametric formulation and (b) direct Gaussian integration formulation. P denotes a generic material property.

illustrated as follows:

$$\text{Displacements } (u, v, w)\text{: e.g.,} \qquad u = \sum_i N_i u_i \quad (102)$$

$$\text{Coordinates } (x, y, z)\text{: e.g.,} \qquad x = \sum_i \tilde{N}_i x_i \quad (103)$$

Material properties (E, v): e.g.,

$$E = \sum_i \bar{N}_i E_i, \quad v = \sum_i \hat{N}_i v_i \quad (104)$$

where N_i, $\tilde{N}_i$, $\bar{N}_i$, and $\hat{N}_i$ are shape functions corresponding to node i, and the summation is done over the element nodal points. Kim and Paulino (2002) have proposed a fully isoparametric element formulation, i.e.,

$$\boldsymbol{N} = \tilde{\boldsymbol{N}} = \bar{\boldsymbol{N}} = \hat{\boldsymbol{N}} \quad (105)$$

This approach interpolates material properties at each Gaussian integration point from the nodal material properties of the element using isoparametric shape functions, which are the same for spatial coordinates and displacements (see Figure 16(a)). An alternative approach is also shown in Figure 16(b) where the material properties are evaluated directly at the Gauss points (Santare and Lambros, 2000). The discussion here presents the generalized isoparametric formulation by Kim and Paulino (2002).

The element stiffness matrix is given by (Cook *et al.*, 1989)

$$\boldsymbol{k}^e = \int_{\Omega_e} \boldsymbol{B}^{e\mathrm{T}} \boldsymbol{D}^e(\boldsymbol{x}) \boldsymbol{B}^e \, \mathrm{d}\Omega_e \quad (106)$$

where $\boldsymbol{u}^e$ is the nodal displacement vector, $\boldsymbol{B}^e$ is the strain–displacement matrix which contains gradients of the interpolating functions, $\boldsymbol{D}^e(\boldsymbol{x})$ is the constitutive matrix, and Ω_e is the domain of element (e). The elasticity matrix $\boldsymbol{D}^e(\boldsymbol{x}) = \boldsymbol{D}^e(x, y)$ becomes a function of spatial coordinates.

The integral in Equation (106) is evaluated by Gaussian quadrature with the matrix $\boldsymbol{D}^e(\boldsymbol{x})$ specified at each Gaussian integration point. Thus, for 2D problems, the resulting integral becomes

$$\boldsymbol{k}^e = \sum_{i=1}^{n} \sum_{j=1}^{n} \boldsymbol{B}_{ij}^{e\mathrm{T}} \boldsymbol{D}_{ij}^e \boldsymbol{B}_{ij}^e J_{ij} w_i w_j \quad (107)$$

where the subscripts i and j refer to the Gaussian integration points, J_{ij} is the determinant of the Jacobian matrix, and w_i are the Gaussian weights. The performance of the graded elements has been investigated by Paulino and Kim (2003) within the context of the weak patch test. The remainder of Section 2.13.4 focuses on 2D problems.

2.13.4.2 SIF Computation

2.13.4.2.1 Displacement correlation technique

The displacement correlation technique (DCT) represents one of the simplest methods to evaluate SIFs. It consists of correlating numerical results for displacement at specific locations on the crack with available analytical solutions. For quarter-point singular elements, the crack opening displacement (COD) profile

at $x=-r$ is given by (Shih *et al.*, 1976)

$$\mathrm{COD}(-r) = (4u_{2,i-1} - u_{2,i-2})\sqrt{\frac{r}{\Delta a}} \qquad (108)$$

where $u_{2,i-1}$ and $u_{2,i-2}$ are the displacements relative to the crack tip in the x_2-direction at locations $(i-1)$ and $(i-2)$, r is the distance from the crack tip along the x_1-direction, and Δa is a characteristic length associated with the crack-tip elements (see Figure 17).

For FGMs, material properties need to be considered at the crack-tip location. Thus, consistent with Equation (23), the analytical expression for $\mathrm{COD}(-r)$, neglecting higher order terms, can be written as

$$\mathrm{COD}(-r) = K_{\mathrm{I}}\left(\frac{\kappa+1}{\mu}\right)_{\mathrm{tip}}\sqrt{\frac{r}{2\pi}} \qquad (109)$$

where $\kappa_{\mathrm{tip}} = 3-4\nu_{\mathrm{tip}}$ for plane strain, $\kappa_{\mathrm{tip}} = (3-\nu_{\mathrm{tip}})/(1+\nu_{\mathrm{tip}})$ for plane stress, and ν_{tip} denotes Poisson's ratio at the crack-tip location. By correlating Equations (108) and (109), the SIF for mode I can be evaluated by

$$K_{\mathrm{I}} = \sqrt{\frac{2\pi}{\Delta a}}\left[4\left(\frac{\mu}{\kappa+1}\right)_{\mathrm{tip}}u_{2,i-1} - \left(\frac{\mu}{\kappa+1}\right)_{\mathrm{tip}}u_{2,i-2}\right] \qquad (110)$$

For mode II, the crack sliding displacement (CSD) replaces the COD and the following expression is readily obtained

$$K_{\mathrm{II}} = \sqrt{\frac{2\pi}{\Delta a}}\left[4\left(\frac{\mu}{\kappa+1}\right)_{\mathrm{tip}}u_{1,i-1} - \left(\frac{\mu}{\kappa+1}\right)_{\mathrm{tip}}u_{1,i-2}\right] \qquad (111)$$

Note that in the above expressions for SIFs, the material properties ($\mu \equiv \mu(\boldsymbol{x})$ and $\kappa \equiv \kappa(\boldsymbol{x})$) have been taken at the crack-tip location consistent with Equation (23). This approach was presented by Kim and Paulino (2002).

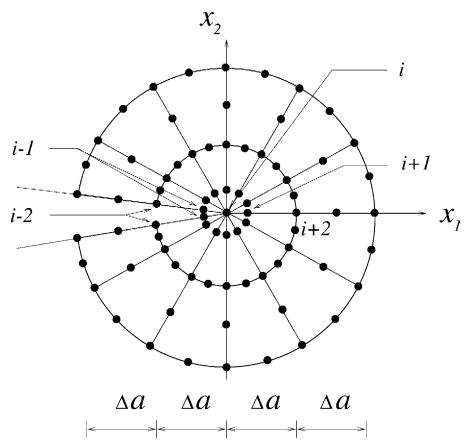

Figure 17 Crack-tip rosette of singular quarter-point (1st ring) and regular (2nd ring) FEs.

2.13.4.2.2 Modified crack-closure integral method

The modified crack-closure integral method (MCC) was proposed by Rybicki and Kanninen (1977) based on Irwin's virtual crack-closure method (Irwin, 1957) using the stresses ahead of the crack tip and the displacements behind the crack tip. The energy release rates can be obtained for modes I and II separately by this method, which utilizes only a single FE analysis. No assumption of isotropy or homogeneity around the crack is necessary. Thus the method is ideally suited for FGMs. The energy release rate is estimated only in terms of the work done by the stresses (or equivalent nodal forces) over the displacements produced by the introduction of a virtual crack extension. The expression for $\mathcal{G}_{\mathrm{I}}$ (strain energy release rate for mode I) and $\mathcal{G}_{\mathrm{II}}$ (strain energy release rate for mode II) may be obtained according to Irwin (1957) as

$$\mathcal{G}_{\mathrm{I}} = \lim_{\delta a\to 0}\frac{2}{\delta a}\int_{x_1=0}^{x_1=\delta a}\frac{1}{2}\sigma_{22}(r=x_1,\ \theta=0,\ a) \times u_2(r=\delta a - x_1,\ \theta=\pi,\ a+\delta a)\,\mathrm{d}x_1 \qquad (112)$$

$$\mathcal{G}_{\mathrm{II}} = \lim_{\delta a\to 0}\frac{2}{\delta a}\int_{x_1=0}^{x_1=\delta a}\frac{1}{2}\sigma_{12}(r=x_1,\ \theta=0,\ a) \times u_1(r=\delta a - x_1,\ \theta=\pi,\ a+\delta a)\,\mathrm{d}x_1 \qquad (113)$$

where $\sigma_{12} \equiv \sigma_{xy}$ and $\sigma_{22} \equiv \sigma_{yy}$ are shear and normal stresses ahead of the crack tip, and $u_1 \equiv u_x$ and $u_2 \equiv u_y$ are the displacements relative to the crack tip coordinates, respectively. Figure 18 illustrates a self-similar virtual crack extension δa and the distribution of normal stress ahead of the crack-tip.

For FGMs, SIFs can be related to the values of the potential energy release rates through the following expressions (Jin and Batra, 1996a):

$$\mathcal{G}_{\mathrm{I}} = \left(\frac{\kappa+1}{8\mu}\right)_{\mathrm{tip}}K_{\mathrm{I}}^2 \quad \text{and} \quad \mathcal{G}_{\mathrm{II}} = \left(\frac{\kappa+1}{8\mu}\right)_{\mathrm{tip}}K_{\mathrm{II}}^2 \qquad (114)$$

Ramamurthy *et al.* (1986) and Raju (1987) have shown that the values of $\mathcal{G}_{\mathrm{I}}$ and $\mathcal{G}_{\mathrm{II}}$ can be written in terms of the equivalent nodal forces $F_2 \equiv F_y$ and $F_1 \equiv F_x$, and the relative nodal displacements u_2 and u_1 when employing quarter-point singular elements around the crack tip (see Figure 17). They provided initial expressions for $\mathcal{G}_{\mathrm{I}}$ and $\mathcal{G}_{\mathrm{II}}$ valid only for pure

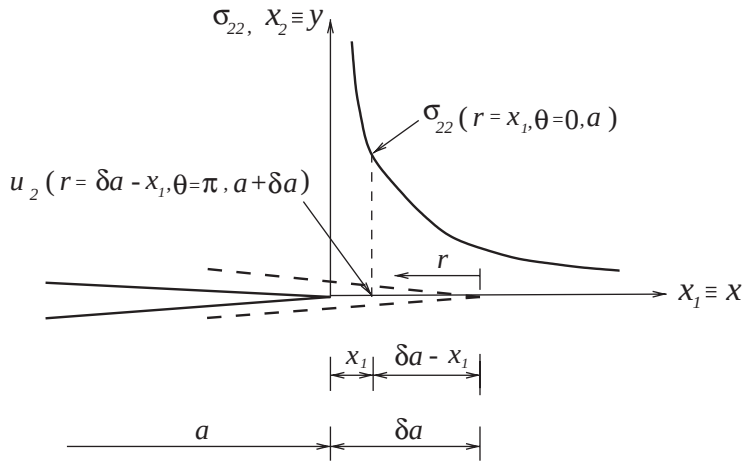

Figure 18 Self-similar crack extension and normal stress distribution.

mode, homogeneous problems. In general, for mixed-mode problems, the deformation is neither symmetric nor antisymmetric about the local x_1 axis. Thus Raju (1987) proposed the corrected formulae, later employed by Kim and Paulino (2002).

2.13.4.2.3 J-integral formulation

Consider 2D deformation cases. The following path-independent J_k^*-integral for general nonhomogeneous materials is established as (Eischen, 1987a; Eischen, 1987b; Kim and Paulino, 2002)

$$J_k^* = \lim_{\Gamma_\varepsilon \to 0} \left\{ \int_{\Gamma_0} \left[W n_k - \sigma_{ij} n_j u_{i,k} \right] \mathrm{d}\Gamma - \int_{\Omega_0} (W_{,k})_{\text{expl}} \, \mathrm{d}\Omega + \int_{\Gamma_c} ([W^+ - W^-] n_k^+ - [S_i^+ u_{i,k}^+ - S_i^- u_{i,k}^-]) \, \mathrm{d}\Gamma \right\} \tag{115}$$

where $W = W(\varepsilon_{ij}, x_i)$ is the strain energy density

$$W = \int_0^{\varepsilon_{ij}} \sigma_{ij} \, \mathrm{d}\varepsilon_{ij} \tag{116}$$

$(W,_k)_{\text{expl}}$ is the "explicit" derivative of W respective to x_k

$$(W,_k)_{\text{expl}} = \frac{\partial}{\partial x_k} W(\varepsilon_{ij}, x_i)|_{\varepsilon_{ij}=\text{const.}, \, x_m=\text{const. for } m \neq k} \tag{117}$$

$S_i = \sigma_{ij} n_j$, Γ_0, $\Gamma_c = \Gamma_c^+ + \Gamma_c^-$, and Ω_0 are illustrated in Figure 19, superscripts $(+)$ and $(-)$ refer to the upper and lower crack faces, and $n_k^+ = -n_k^-$ is the outward unit normal vector to Γ_c^+. The notation $[W^+ - W^-]$ denotes the discontinuity (or jump) in the strain energy

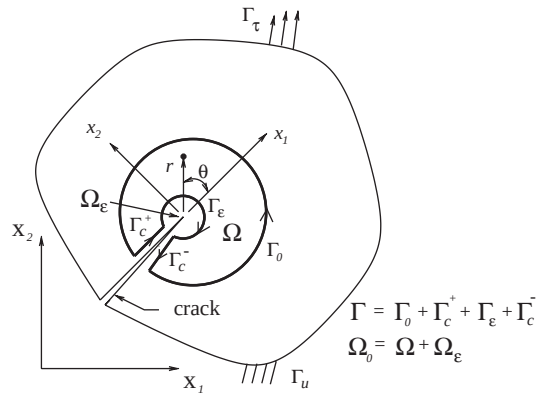

Figure 19 Schematic of a cracked body.

density across the crack opening. Notice that the material nonhomogeneity affects the standard J-integral (Rice, 1968) by adding an area integral term involving the derivative of the strain energy density. This term must be included to allow computation over relatively large regions to evaluate the J-integral using the FEM.

By introducing the equivalent domain integral (EDI) (Raju and Shivakumar, 1990; Gu *et al.*, 1999), Kim and Paulino (2002) converted the closed contour integral of Equation (115) to the following expression if the crack surfaces remain traction free:

$$J_k^* = \int_A [\sigma_{ij} u_{i,k} - W \delta_{kj}] q_{,j} \, \mathrm{d}A - \int_A (W,_k)_{\text{expl}} q \, \mathrm{d}A + \int_{\Gamma_c} [W^+ - W^-] q n_k^+ \, \mathrm{d}\Gamma \tag{118}$$

where q is a smooth function which has the value of unity on Γ_ε and zero on Γ_0. The two often-used shapes of the q function are the pyramid function and the plateau function, the latter being illustrated by Figure 20. All the

details about the computational implementation of J_k^*-integral can be found in the paper by Kim and Paulino (2002).

The relation among the two components ;of the J_k^*-integral and the mode I and II SIFs is established for plane stress as (Eischen, 1987a)

$$J_1^* = \frac{K_I^2 + K_{II}^2}{E_{tip}} \tag{119}$$

$$J_2^* = \frac{-2K_I K_{II}}{E_{tip}} \tag{120}$$

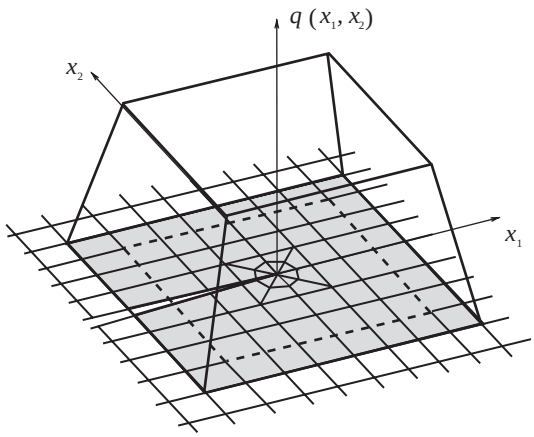

Figure 20 Plateau weight function (q function) used in the EDI implementation of J_k^*.

For plane strain, the Young modulus at the crack-tip E_{tip} must be divided by $(1 - v_{tip}^2)$, where v_{tip} denotes Poisson's ratio at the crack tip.

2.13.4.2.4 Examples

The FEM has been used to calculate SIFs for FGMs in a number of publications by, for example, Anlas *et al.* (2000), Bao and Wang (1995), Marur and Tippur (2000a, 2000b), and Rousseau and Tippur (2000, 2001). Here we only describe a few examples by Kim and Paulino (2002).

(i) Three-point bending specimen with crack perpendicular to material gradation

Marur and Tippur (1998) have fabricated FGM specimens using a gravity assisted casting technique with two-part slow curing epoxy and uncoated solid glass sphere fillers. They have also analyzed a three-point bending specimen with a crack normal to the elastic gradient using both experimental (static fracture tests) and numerical (FEM) techniques (Marur and Tippur, 2000b). Figure 21(a) shows the specimen geometry and boundary conditions (BCs). Figure 21(b) shows linear variation of Young's modulus in the material gradient region from 10.79 GPa to 3.49 GPa, and the linear variation of Poisson's ratio from

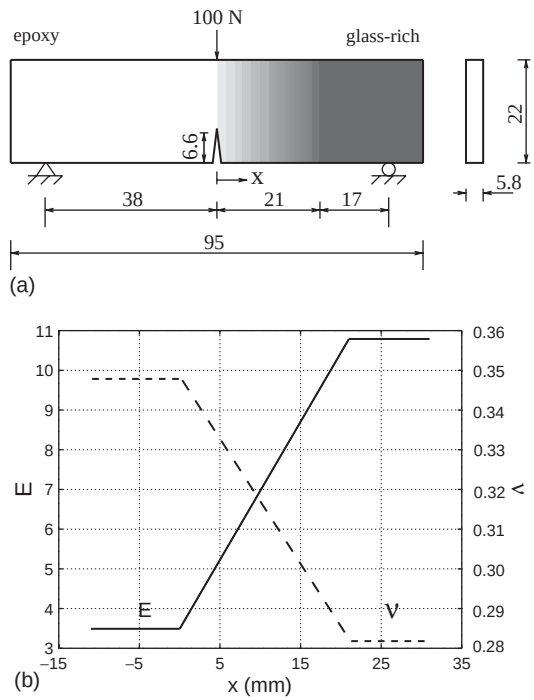

Figure 21 Three-point bending specimen with crack perpendicular to the material gradation: (a) specimen geometry (length in mm) and (b) variation of Young's modulus and Poisson's ratio (all dimensions in mm).

0.348 on the epoxy side to 0.282 on the glass-rich side. Figure 22 shows the detail of the mesh using 16 sectors (S16) and 4 rings (R4) around the crack tip. Marur and Tippur (2000b) used the experimental strain data to compute $|\boldsymbol{K}| = 0.65\,\text{MPa}\,\text{m}^{1/2}$ and $\psi = -3.45^\circ$, while their FEM results are $|\boldsymbol{K}| = 0.59\,\text{MPa}\,\text{m}^{1/2}$ and $\psi = -3.24^\circ$, where $\psi = \tan^{-1}(K_{\text{II}}/K_{\text{I}})$ is the mode-mixity parameter. Table 4 lists these numerical results together with the present ones obtained using MCC, DCT, and J_k^*-integral, which are in reasonable agreement with each other.

(ii) Multiple interacting cracks in a plate

Figure 23(a) shows two cracks each of length $2a$ located with the angle θ_I ($\theta_1 = 30^\circ$, $\theta_2 = 60^\circ$) in a finite 2D plate. Figure 23(b) shows the complete FEM mesh, and Figures 23(c) and 23(d) show details of the center region and around crack tips, respectively. The distance from the origin to the two crack tips is 1.0. Shbeeb *et al.* (1999a, 1999b) have provided semianalytical solutions for this example obtained with the integral equation method. However, the graphical results given in their paper makes accurate verification difficult. The applied load corresponds to $\sigma_{22}(x_1, 10) = \sigma_0 = 1.0$. This stress distribution was obtained by applying nodal forces along the top edge of the mesh. The displacement boundary condition is prescribed such that $u_2 = 0$ along the lower edge and, in addition, $u_1 = 0$ for the node at the left-hand side. Young's modulus is an exponential function of x_2, while Poisson's ratio remains constant equal to zero in this numerical analysis. The paper by Shbeeb *et al.* (1999b) did not specify the actual value of Poisson's ratio. Eight-node serendipity elements (Q8) are used over most of the mesh, while at each crack tip, quarter-point six-node triangles (T6qp) were used. The mesh has 2287 Q8 and 214 T6 with a total of 2501 elements and 7517 nodes. The following data are used for the FE analysis: $2a = 2$; $L/W = 1.0$; $E(x_2) = \bar{E}e^{\beta x_2}$; $\bar{E} = 1.0$; $\beta a = (0.0,\ 0.25,\ 0.5,\ 0.75,\ 1.0)$; $v = 0.0$; generalized plane stress; and 2×2 Gauss quadrature. With this geometrical configuration, the material property E grows quite large as the plate size increases. However, this is just an artifact of the modeling, which occurs because the nonhomogeneity parameter β introduces a geometrical length scale ($1/\beta$) into the problem. The relevant material variation is that around the crack region

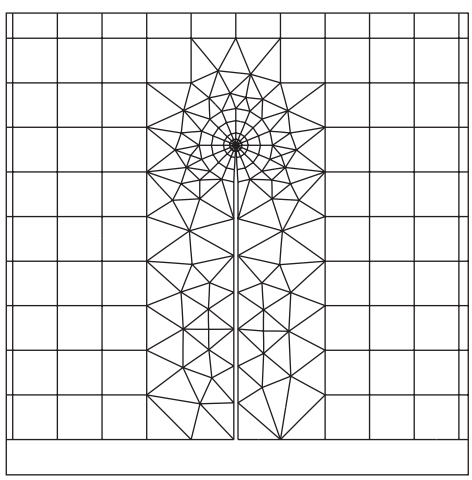

Figure 22 FE mesh for three-point bending specimen with crack perpendicular to the material gradation: detail around the crack tip showing 16 sectors and 4 rings of elements.

The geometrical configuration for this problem approximates the infinite plate as originally conceived by Shbeeb *et al.* (1999b). Table 5 shows a comparison of the normalized SIFs at the two crack tips for the lower crack with the angle $\theta = 30^\circ$ computed by using the DCT, MCC, and the J_k^*-integral with those reported by Shbeeb *et al.* (1999b). In this table $K_{\text{I}}(a^-)$ and $K_{\text{I}}(a^+)$ refer to the SIFs at the left and right crack tips, respectively. Similar notation is adopted for K_{II}. Both the DCT and J_k^*-integral based values agree reasonably well with the results by Shbeeb *et al.* (1999b), and the MCC provides the best estimates for the SIFs.

2.13.4.3 Cohesive Zone Modeling

Cohesive fracture models have been widely used to simulate and analyze crack growth in ductile and quasibrittle materials. In a cohesive fracture model, a narrow band termed a

Table 4 FEM SIFs for three-point bending specimen with crack perpendicular to material gradation.

	Kim and Paulino (2002)			
Parameters	*MCC*	J_k^*-integral	*DCT*	*Marur and Tippur (2000b)*
K_{I}	0.557	0.557	0.558	0.589
K_{II}	–0.028	–0.026	–0.026	–0.033
$\lvert\mathbf{K}\rvert$	0.5575	0.5576	0.5580	0.59
ψ	-2.87°	-2.67°	-2.64°	-3.24°

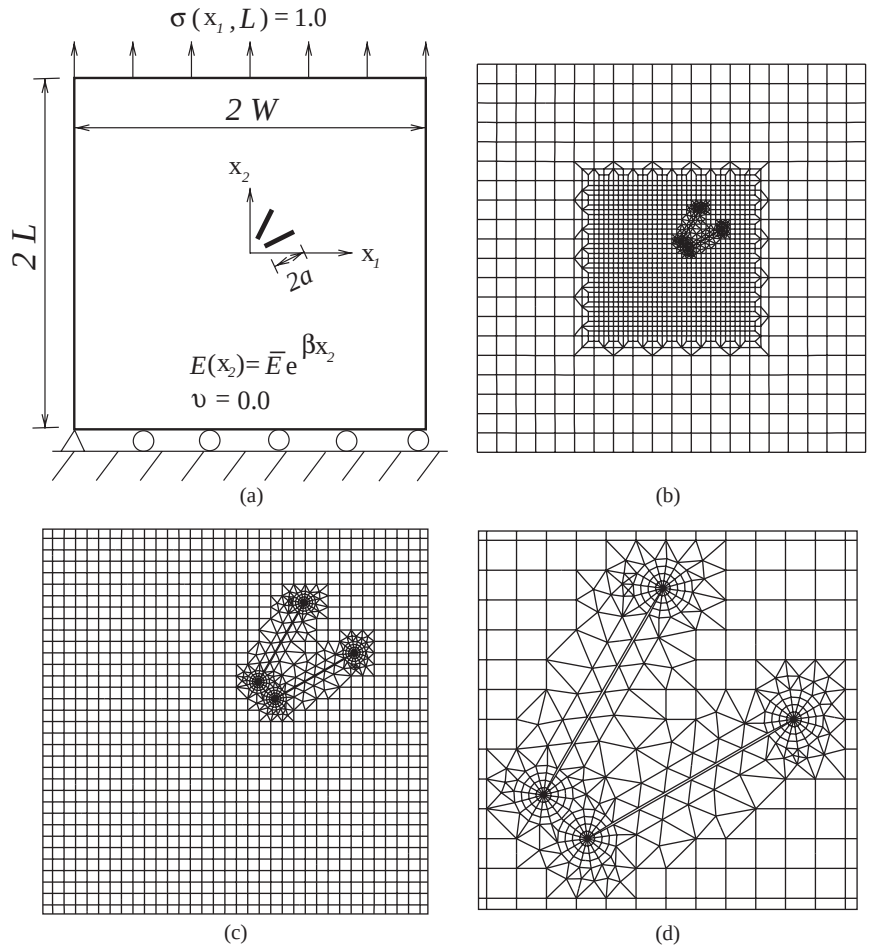

Figure 23 Two interacting cracks in a plate: (a) geometry and BCs; (b) FE mesh; (c) mesh detail of center region and (d) mesh detail around crack tips showing 16 sectors (S16) and four rings (R4) of elements around each tip.

cohesive zone, or process zone, exists ahead of the crack front. Material behavior in the cohesive zone follows a cohesive constitutive law which relates the cohesive traction to the relative displacements of the adjacent surfaces. Crack growth then occurs by progressive decohesion of the cohesive surfaces. Though cohesive fracture models have been successfully employed to simulate failure processes in homogeneous materials and conventional composites, few studies have extended the concept to FGMs. Generalization of the cohesive zone concept to model fracture in FGMs represents a challenging task in view of the different failure mechanisms present in an FGM. In a typical ceramic/metal FGM, the ceramic-rich region may be regarded as a metal-particle-reinforced ceramic-matrix composite, whereas the metal-rich region may be treated as a ceramic-particle-reinforced metal-matrix composite (see discussion on micromechanics models in Section 2.13.2.2). Though models for the failure mechanisms of conventional composites may be adopted to study the fracture processes in the ceramic-rich or metal-rich region, the failure mechanisms operative in the interconnecting region which has no distinct matrix and inclusion phases remain unknown. This section describes a new volume-fraction-based, phenomenological cohesive fracture model (Jin *et al.*, 2002) and crack-growth analysis results obtained using the model.

2.13.4.3.1 A cohesive zone model

Consider general 3D mixed-mode fracture problems. In a 3D setting, Camacho and Ortiz (1996) have introduced an effective displacement jump across the cohesive surfaces, δ_{eff}, and an effective cohesive traction, σ_{eff}, as follows:

$$\delta_{\text{eff}} = \sqrt{\delta_n^2 + \eta^2 \delta_s^2} \tag{121}$$

$$\sigma_{\text{eff}} = \sqrt{\sigma_n^2 + \eta^{-2} \sigma_s^2} \tag{122}$$

Table 5 Normalized SIFs for lower crack ($K_0 = \sigma_{22}\sqrt{\pi a}$).

Method	β	$K_I(a^-)/K_0$	$K_{II}(a^-)/K_0$	$K_I(a^+)/K_0$	$K_{II}(a^+)/K_0$
Shbeeb *et al.* (1999b) (approximate)	0.00	0.59	0.43	0.78	0.42
	0.25	0.62	0.39	0.82	0.48
	0.50	0.66	0.36	0.88	0.57
	0.75	0.69	0.34	0.98	0.685
MCC	0.00	0.589	0.423	0.804	0.408
	0.25	0.626	0.385	0.816	0.474
	0.50	0.662	0.346	0.842	0.546
	0.75	0.696	0.312	0.880	0.625
J_k^*-integral	0.00	0.603	0.431	0.801	0.431
	0.25	0.627	0.401	0.811	0.495
	0.50	0.662	0.363	0.841	0.558
	0.75	0.692	0.347	0.895	0.617
DCT	0.00	0.598	0.413	0.812	0.399
	0.25	0.632	0.375	0.818	0.463
	0.50	0.672	0.336	0.838	0.533
	0.75	0.712	0.302	0.869	0.610

After Kim and Paulino (2002).

where δ_n and δ_s are the normal and tangential displacement jumps across the cohesive surfaces, σ_n and σ_s are the normal and shear cohesive tractions, and the parameter η assigns different weights to the opening and sliding displacements (η is usually taken as $\sqrt{2}$). Here we assume that resistance of the cohesive surfaces to relative sliding is isotropic in the cohesive (tangent) plane so that

$$\delta_s = \sqrt{\delta_{s1}^2 + \delta_{s2}^2} \tag{123}$$

$$\sigma_s = \sqrt{\sigma_{s1}^2 + \sigma_{s2}^2} \tag{124}$$

in which δ_{s1} and δ_{s2} are the two relative sliding displacements across the cohesive surfaces, and σ_{s1} and σ_{s2} are the two shear cohesive tractions.

With the introduction of the above effective traction and displacement, a free energy potential is assumed to exist in the following volume-fraction-based form (Jin *et al.*, 2002)

$$\phi(\boldsymbol{x}, \delta_{\text{eff}}, q) = \frac{V_{\text{met}}(\boldsymbol{x})}{V_{\text{met}}(\boldsymbol{x}) + \beta_{\text{met}}[1 - V_{\text{met}}(\boldsymbol{x})]}\phi_{\text{met}}(\delta_{\text{eff}}, q) + \frac{1 - V_{\text{met}}(\boldsymbol{x})}{1 - V_{\text{met}}(\boldsymbol{x}) + \beta_{\text{cer}} V_{\text{met}}(\boldsymbol{x})}\phi_{\text{cer}}(\delta_{\text{eff}}, q) \tag{125}$$

where $V_{\text{met}}(\boldsymbol{x})$ denotes the volume fraction of the metal, β_{met} (≥ 1) and β_{cer} (≥ 1) represent the two cohesive gradation parameters, $\boldsymbol{x} = (x_1, x_2, x_3)$, q is an internal variable describing the irreversible processes of decohesion, and ϕ_{met} and ϕ_{cer} are the free energy potentials for the metal and ceramic phases, respectively, given by

$$\phi_{\text{met}}(\delta_{\text{eff}}, q) = e\sigma_{\text{met}}^{\text{c}}\delta_{\text{met}}^{\text{c}}\left[1 - \left(1 + \frac{\delta_{\text{eff}}}{\delta_{\text{met}}^{\text{c}}}\right)\exp\left(-\frac{\delta_{\text{eff}}}{\delta_{\text{met}}^{\text{c}}}\right)\right] \tag{126}$$

$$\phi_{\text{cer}}(\delta_{\text{eff}}, q) = e\sigma_{\text{cer}}^{\text{c}}\delta_{\text{cer}}^{\text{c}}\left[1 - \left(1 + \frac{\delta_{\text{eff}}}{\delta_{\text{cer}}^{\text{c}}}\right)\exp\left(-\frac{\delta_{\text{eff}}}{\delta_{\text{cer}}^{\text{c}}}\right)\right] \tag{127}$$

where $e = \exp(1)$, $\sigma_{\text{met}}^{\text{c}}$ is the maximum cohesive traction of the metal phase, $\delta_{\text{met}}^{\text{c}}$ the value of δ_{eff} at $\sigma_{\text{eff}} = \sigma_{\text{met}}^{\text{c}}$, $\sigma_{\text{cer}}^{\text{c}}$ the maximum cohesive traction of the ceramic phase, and $\delta_{\text{cer}}^{\text{c}}$ the value of δ_{eff} at $\sigma_{\text{eff}} = \sigma_{\text{cer}}^{\text{c}}$, as illustrated by Figure 24.

The effective cohesive traction is then obtained from the above potential as follows:

$$\begin{aligned}\sigma_{\text{eff}} &= \frac{\partial \phi}{\partial \delta_{\text{eff}}} \\ &= \frac{V_{\text{met}}(\boldsymbol{x})}{V_{\text{met}}(\boldsymbol{x}) + \beta_{\text{met}}[1 - V_{\text{met}}(\boldsymbol{x})]}e\sigma_{\text{met}}^{\text{c}}\left(\frac{\delta_{\text{eff}}}{\delta_{\text{met}}^{\text{c}}}\right) \\ &\quad \times \exp\left(-\frac{\delta_{\text{eff}}}{\delta_{\text{met}}^{\text{c}}}\right) \\ &\quad + \frac{1 - V_{\text{met}}(\boldsymbol{x})}{1 - V_{\text{met}}(\boldsymbol{x}) + \beta_{\text{cer}} V_{\text{met}}(\boldsymbol{x})}e\sigma_{\text{cer}}^{\text{c}}\left(\frac{\delta_{\text{eff}}}{\delta_{\text{cer}}^{\text{c}}}\right) \\ &\quad \times \exp\left(-\frac{\delta_{\text{eff}}}{\delta_{\text{cer}}^{\text{c}}}\right) \\ &\quad \text{if } \delta_{\text{eff}} = \delta_{\text{eff}}^{\max} \text{ and } \dot{\delta}_{\text{eff}} \geq 0\end{aligned} \tag{128}$$

for the loading case, and

$$\sigma_{\text{eff}} = \left(\frac{\sigma_{\text{eff}}^{\max}}{\delta_{\text{eff}}^{\max}}\right)\delta_{\text{eff}}, \quad \text{if } \delta_{\text{eff}} < \delta_{\text{eff}}^{\max} \text{ or } \dot{\delta}_{\text{eff}} < 0 \tag{129}$$

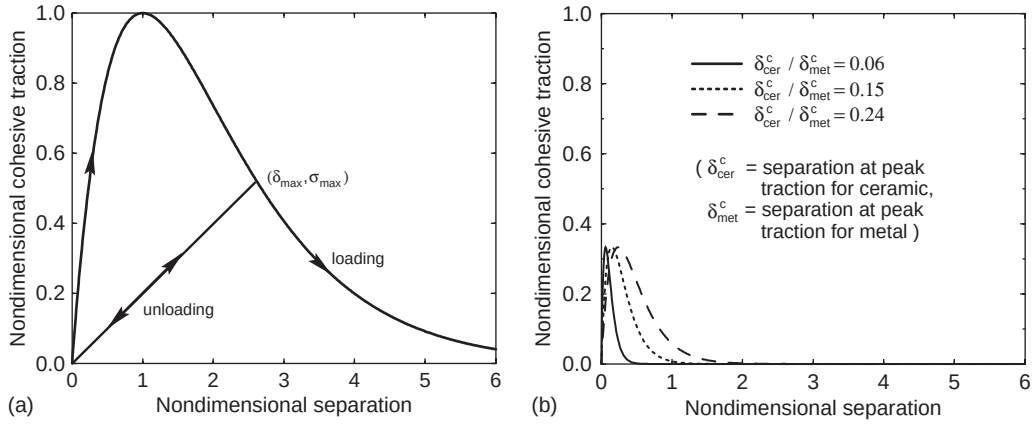

Figure 24 Normalized cohesive traction versus nondimensional separation displacement: (a) for metal, $\sigma_{\text{met}}/\sigma^{\text{c}}_{\text{met}}$ versus $\delta/\delta^{\text{c}}_{\text{met}}$ and (b) for ceramic, $\sigma_{\text{cer}}/\sigma^{\text{c}}_{\text{met}}$ versus $\delta/\delta^{\text{c}}_{\text{met}}$ (where metal/ceramic strength ratio, $\sigma^{\text{c}}_{\text{met}}/\sigma^{\text{c}}_{\text{cer}}$, is taken to be 3).

for the unloading case, where $\sigma^{\max}_{\text{eff}}$ is the value of σ_{eff} at $\delta_{\text{eff}} = \delta^{\max}_{\text{eff}}$ calculated from Equation (128). Here, the internal variable q is chosen as $\delta^{\max}_{\text{eff}}$, the maximum value of δ_{eff} attained. The cohesive law for general 3D deformations is then formulated as follows:

$$\sigma_n = \frac{\partial \phi}{\partial \delta_n} = \frac{\partial \phi}{\partial \delta_{\text{eff}}}\frac{\partial \delta_{\text{eff}}}{\partial \delta_n} = \left(\frac{\sigma_{\text{eff}}}{\delta_{\text{eff}}}\right)\delta_n$$
$$\sigma_s = \frac{\partial \phi}{\partial \delta_s} = \frac{\partial \phi}{\partial \delta_{\text{eff}}}\frac{\partial \delta_{\text{eff}}}{\partial \delta_s} = \eta^2\left(\frac{\sigma_{\text{eff}}}{\delta_{\text{eff}}}\right)\delta_s \tag{130}$$

Compared with the formulation for homogeneous materials, the FGM cohesive fracture model, given by Equations (128)–(130), increases the number of material-dependent parameters by two (β_{met}, β_{cer}). Values for the local separation energies and peak cohesive tractions related to the pure ductile and brittle phases are obtained using standard procedures for homogeneous materials (see Roy and Dodds (2001) for example). The material-dependent parameters β_{met} and β_{cer} describe approximately the overall effect of cohesive traction reduction (from the level predicted by the rule of mixtures) and the transition between the fracture mechanisms of the metal and ceramic phases. The preliminary analyses of crack growth in ceramic/metal FGMs by Jin *et al.* (2002) indicate that β_{met} plays a far more significant role than β_{cer}, which can be simply set to unity. It is anticipated that the parameter β_{met} may be experimentally calibrated by two different procedures. The first procedure determines β_{met} by matching the predicted and measured crack growth responses in standard fracture mechanics specimens of FGMs. Instead of using FGM specimens, the second procedure employs fracture specimens made of a monolithic composite each with a fixed volume fraction of the constituents. This opens the potential to calibrate β_{met} for each volume fraction level of metal and ceramic, which comprise the FGM specimens, i.e., β_{met} can become a function of V_{met} in the present model.

2.13.4.3.2 Cohesive element

Figure 25 illustrates the 3D interface cohesive element where (x_1, x_2, x_3) are the global cartesian coordinates, (s_1, s_2, n) are the element-specific, local Cartesian coordinates, and (η, ζ) are the parametric coordinates. The interface-cohesive element consists of two four-node bilinear isoparametric surfaces. Nodes 1–4 lie on one surface of the element with nodes 5–8 on the opposite surface. The two surfaces initially occupy the same location. When the whole body deforms, the two surfaces undergo both normal and tangential displacements relative to each other. The cohesive tractions corresponding to the relative displacements follow the constitutive relations Equations (128)–(130), and thus maintain the two surfaces in a ''cohesive'' state.

The tangent stiffness matrix of the cohesive element is given by (Roy and Dodds, 2001)

$$\boldsymbol{K}_{\text{T}} = \int_{-1}^{1}\int_{-1}^{1} \boldsymbol{B}^{\text{T}}_{\text{coh}}\boldsymbol{D}_{\text{coh}}\boldsymbol{B}_{\text{coh}}J_0\,\text{d}\eta\,\text{d}\zeta \tag{131}$$

where $\boldsymbol{B}_{\text{coh}}$ extracts the relative displacement jumps within the cohesive element from the nodal displacements, J_0 is the Jacobian of the transformation between parametric (η, ζ) and Cartesian coordinates (s_1, s_2) in the tangent plane of the cohesive element, and $\boldsymbol{D}_{\text{coh}}$ is the tangent modulus matrix of the cohesive law Equations (128)–(130) (Jin *et al.*, 2002). For FGMs, the $\boldsymbol{D}_{\text{coh}}$ matrix depends on spatial position through the graded volume fraction of

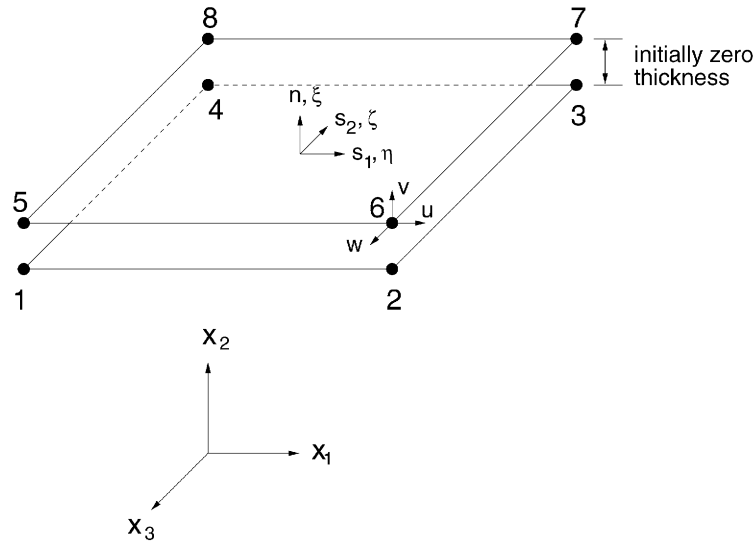

Figure 25 Eight-node bilinear interface element.

Table 6 Material properties of Ti and TiB.

Materials	E (GPa)	ν	J_c (KJ/m^2)	σ^c_{met} (MPa)	δ^c_{met} (mm)	σ^c_{cer} (MPa)	δ^c_{cer} (mm)
Ti	107	0.34	150	620	0.089		
TiB	375	0.14	0.11			4.0	0.01

the metal phase, V_{met}, in a ceramic/metal FGM. V_{met} is approximated by the standard interpolation

$$V_{met} = \sum_{i=1}^{4} N_i V^i_{met} \tag{132}$$

where $V^i_{met}(i = 1, 2, 3, 4)$ are the values of V_{met} at the nodal points of the interface-cohesive elements and $N_i(\xi, \eta, \zeta)$ $(i = 1, 2, \ldots, n)$ the standard shape functions. The present formulation is fully isoparametric (Kim and Paulino, 2002).

2.13.4.3.3 Cohesive fracture simulation

Numerical analyses of crack growth for both compact tension, C(T), and single-edge notch bend, SE(B), specimens of a titanium/titanium monoboride (Ti/TiB) FGM have been performed in Jin *et al.* (2002). The material properties for the Ti and TiB are summarized in Table 6. The Young's modulus and Poisson's ratio of the Ti/TiB FGM are estimated by the self-consistent method (Hill, 1965).

Figure 26 illustrates the SE(B) specimen geometry and Table 7 provides the geometric parameters for the SE(B) specimen. A layered FGM version of the SE(B) specimen has been tested in Carpenter *et al.* (1999). From a modeling point of view, the FGM composition varies from 100% TiB at the cracked surface to 100% Ti at the uncracked surface. Thus the volume fraction of Ti varies from zero at the cracked surface to one at the uncracked surface.

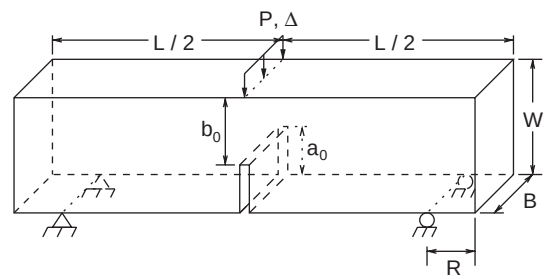

Figure 26 SE(B) specimen geometry.

Table 7 Geometric parameters of SE(B) specimen.

Specimen	L (mm)	W (mm)	B (mm)	a_0/W	R (mm)
SE(B)	79.4	14.7	7.4	0.3	10.2

The finite element models consist of eight-node isoparametric solid elements and the eight-node interface-cohesive elements. Due to

symmetry considerations, only one-quarter of the specimen is considered. Interface-cohesive elements are placed only over the initial uncracked ligament and have a uniform length of 0.1 mm for the SE(B) specimen. The finite element model has 10 uniform layers of elements over the half thickness for the SE(B) specimen. Figure 27 shows the front view of the finite element mesh for the SE(B) specimen.

The SE(B) specimen is loaded by opening displacements applied uniformly through the thickness at the specimen center plane. In the layered FGM SE(B) specimen tested (Carpenter *et al.*, 1999), the first layer of the specimen consists of 15% Ti and 85% TiB, while the last layer (7th layer) consists of 100% Ti. Crack initiation occurred at a measured load of 920 Newtons (N). The experimental results show that load increases with crack extension during the initial growth and then decreases with further crack extension. The measured load corresponding to a crack growth of 5 mm is $\sim$1200 N. Figure 28(a) shows the volume fraction of Ti in this TiB/Ti specimen. The dotted (stepped) line shows the property gradation in the tested specimen. A least-squares approximation yields the power exponent $n = 0.84$ in the metal volume fraction function used in the analysis

$$V_{\text{met}}(Y) = (Y/W)^n \tag{133}$$

Figure 28(b) shows the numerical results of the load versus crack extension responses for the SE(B) specimen with $\beta_{\text{met}} = 16$ and $n = 0.84$. For the β_{met} selected, the crack initiation load agrees quite closely with the experimentally measured value. Compared with the experimental observations after the crack initiation (Carpenter *et al.*, 1999), the discrepancy in the trend of load versus crack extension response arises because the finite element analysis does not consider plasticity in the background material. When the plasticity effect is taken into account, it is expected that the trend of the load versus crack extension will be more consistent with the experimental observations

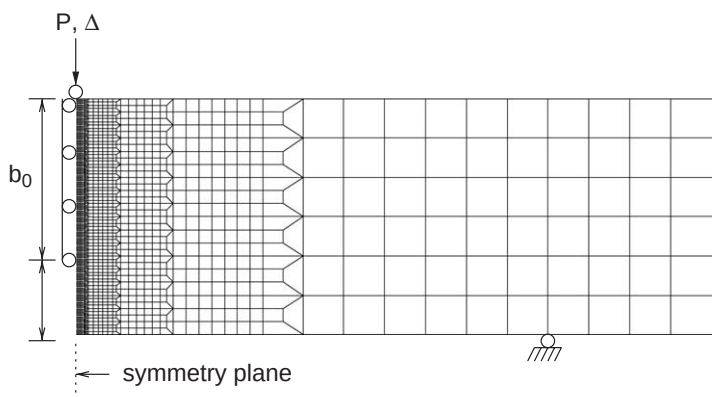

Figure 27 Typical mesh for analyses of SE(B) specimen (longitudinal center plane of the quarter-symmetric 3D model).

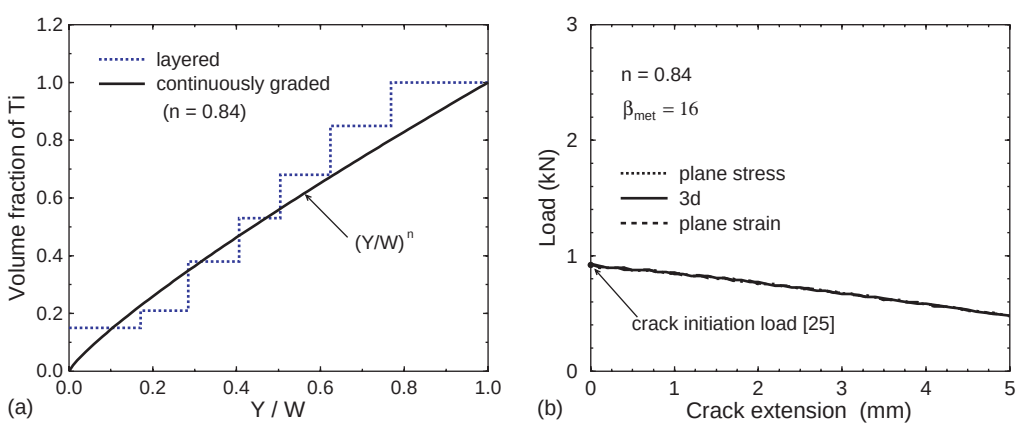

Figure 28 (a) Volume fraction of Ti in the TiB/Ti FGM and (b) load-crack extension response for the SE(B) Ti/TiB specimen with $a_0/W = 0.3$, $B = 7.4$ mm, $n = 0.84$ (after Jin *et al.*, 2002).

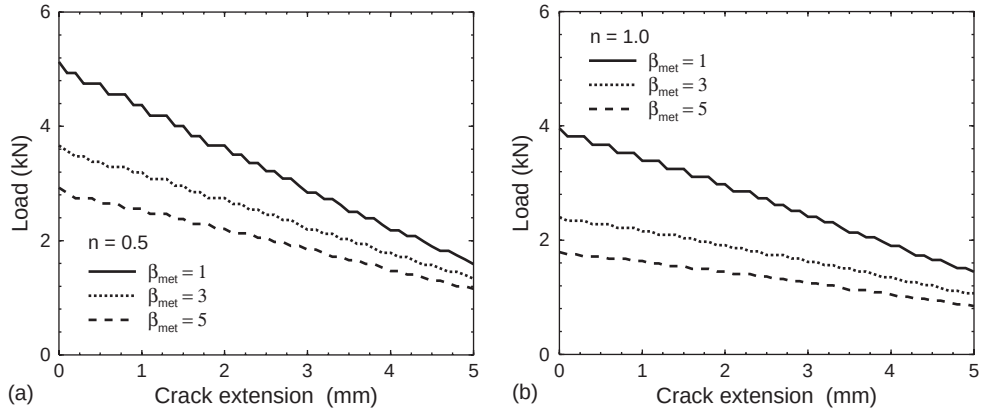

Figure 29 Load-crack extension response for the SE(B) Ti/TiB specimen with $a_0/W = 0.3$, $B = 7.4$ mm: (a) $n = 0.5$ and (b) $n = 1.0$ (after Jin *et al.*, 2002).

(the calibrated value of β_{met} may be larger than 16). Figure 28(b) also shows the numerical results of the load versus crack extension for plane-stress and plane-stress models. Although there are no differences between the 2D and 3D responses, it is expected that significant differences may develop with plasticity in the background material due to variations in crack front constraint and crack front tunneling.

Figure 29 shows the effect of β_{met} and n on the load versus crack extension responses for the SE(B) specimen. The power exponent n (shape index of the metal volume fraction) is 0.5 in Figure 29(a) and 1.0 in Figure 29(b). For a given β_{met}, the load decreases steadily with crack extension. For a given crack extension, a larger β_{met} reduces the load. This is expected because a larger β_{met} corresponds to a lower cohesive traction. Finally, the load becomes lower for larger n. This is because a larger n means a lower metal volume fraction, and therefore, a lower cohesive traction. Because β_{met} has a pronounced effect on the load versus crack extension responses, one may expect to calibrate the values of β_{met} from experimental observations.

2.13.5 SOME EXPERIMENTAL ASPECTS

Fracture experiments play a critical role to develop an understanding of the influence of property gradients on the mechanisms of crack growth and on the fracture toughness of these materials. In addition, carefully designed fracture experiments are needed to calibrate the parameters used in numerical methods (see, e.g., Section 2.13.4.3.3). The presentation below focuses on fracture testing of engineering FGMs (e.g., metal/ceramic) with particular emphasis on an effective technique to generate a sharp precrack in those materials.

2.13.5.1 Metal/Ceramic FGM Fracture Specimen

A functionally graded Ti/TiB material was prepared by Cercom Incorporated, Vista, CA, using a commercially pure (CP) titanium plate and six tape-cast mixtures of titanium (Ti) and titanium diboride (TiB_2) powders (Nelson and Ezis, 1996). The assembled green material was placed in a graphite die in an induction furnace and heated to 500°C in vacuum to remove organic tape materials. The material was then heated further to 1,100°C to remove surface-absorbed gases from TiB_2 and then heated to 1,305°C under a pressure of 13.8 MPa. Subsequent X-ray diffraction revealed that reactions between Ti and TiB_2 during the 36 h pressing and cooling time resulted in the formation of titanium monoboride (TiB) with less than 1% of residual TiB_2. The compositions of the layers in the FGM varied from 15%Ti/85%TiB on the brittle side to pure Ti on the ductile side. The intermediate compositions of the FGM were chosen to reduce the thermal residual stress during cooling from the sintering temperature as described by Gooch *et al.* (1999). Single-edged-notched bend specimens (SE(B)) of the FGM were cut using electro-discharge machining (EDM) with the machined notch on the side containing the highest concentration of TiB. The notch was oriented for crack propagation through the layers toward the CP–Ti. The specimens were machined to a width of 14.73 mm, a thickness of 7.37 mm and a length of 82.55 mm, with a notch 5.08 mm deep (initial $a/W = 0.345$) with integral clip gage knife-edges in accordance with ASTM E1820-96 (ASTM, 1996), as illustrated by Figure 30.

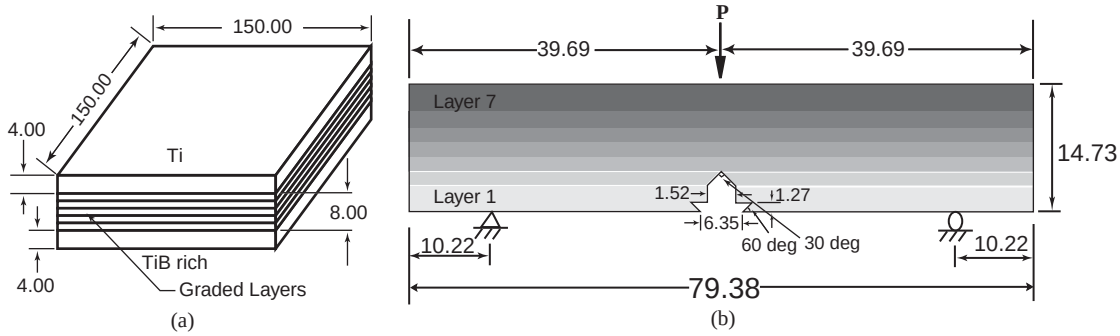

Figure 30 Seven-layer Ti/TiB FGM: (a) plate provided by CERCOM Inc. and (b) fracture specimen (7.37 mm thick) cut from the plate for three-point bending test.

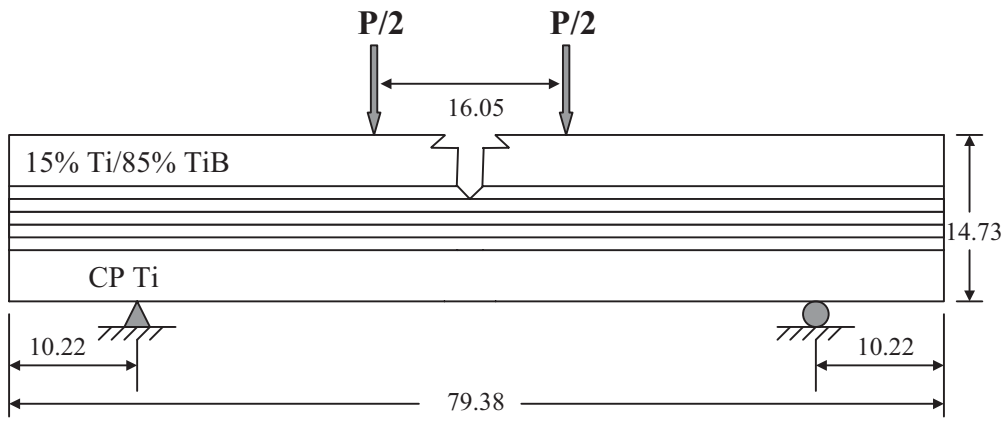

Figure 31 Seven-layer Ti/TiB reverse four-point bending specimen. The composition for each layer is (1) 15/85, (2) 21/79. (3) 38/62, (4) 53/47, (5) 68/32, (6) 85/15, and (7) 100/0 where the number in parentheses indicates the layer number (all dimensions in mm, after Carpenter *et al*., 2000).

2.13.5.2 Precracking of Metal/Ceramic FGMs

In metal/ceramic FGMs, cracks originating in the brittle, ceramic side are prevented from catastrophic propagation through the increase in fracture toughness as the metal content increases. Fracture toughness testing of metallic/ceramic FGM SE(B), with the starting notch in the ceramic-rich side, requires the initiation of a sharp, short precrack at a specific desired location in a brittle material. A review of fracture toughness testing of brittle materials by Sakai and Bradt (1993) notes that creation of a starter crack of proper sharpness and length is critical for accurate fracture toughness measurements. The standard for fracture toughness testing of advanced ceramic materials describes the requirement of a sharp, well-characterized precrack as well as the difficulty in obtaining one (ASTM, 1997). Use of machined notches or blunt cracks can lead to fracture toughness values much larger than those obtained from specimens with sharp precracks. The single edge precracked beam (SEPB) method, based on standard four-point bending with the notch tip in tension, can lead to longer than desired popped-in precracks in multilayered FGMs (Carpenter *et al*., 2000) even when a rigid testing machine limits displacement. Long precracks can also give values of fracture toughness that are too high due to crack wake effects. The method of axial compression precracking developed by Ewart and Suresh (1986) for ceramic materials can lead to extensive microstructural damage in metallic/ceramic FGMs and can give low values of fracture toughness (Carpenter, 1999). Below we describe a method for generating a short, sharp precrack at the root of a machined notch in the brittle side of an FGM due to Carpenter *et al*. (2000), and the technique is illustrated with a Ti/TiB FGM.

2.13.5.3 Precracking by Reverse Four-point Bending

The SE(B) specimens were cyclically loaded in reverse four-point bending using a 6,800 N

load, resulting in initiation of a controlled, short, sharp crack at the machine notch. The loading configuration of the specimens is shown in Figure 31. The load was applied with a compressive load ratio ($R = 10$) at a cyclic frequency of 5 Hz. The load was chosen to develop the precrack in ~5,000 cycles. The target crack length was 0.2 mm from the starting notch which gave the desired $a/W = 0.358$ for the fracture experiments. The starting notch and resulting precrack developed by reverse four-point bending fatigue are shown by optical micrographs, Figures 32(a) and (b), respectively. Average modulus values, measured before and after the precracking were 145 GPa, indicating that the overall microstructure of the FGM was undamaged by reverse four-point bending. After heat tinting at 400°C, the specimens were cooled overnight to room temperature and fracture tested in three-point bending according to ASTM E1820-96 (ASTM, 1996).

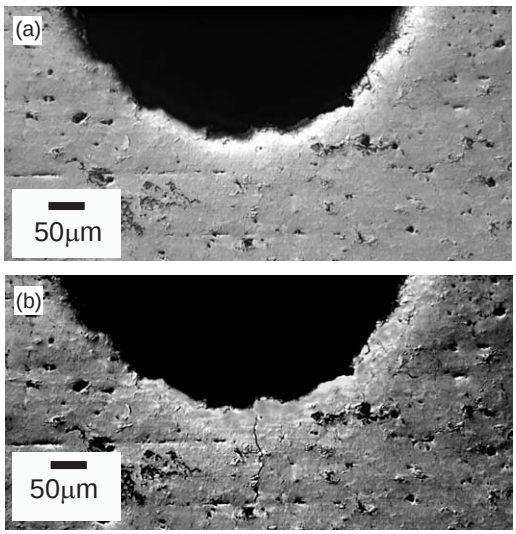

Figure 32 Face of FGM SE(B) specimen: (a) before precracking and (b) precracked in reverse four-point bending fatigue (after Carpenter *et al.*, 2000).

2.13.5.4 Test Results

The load versus CMOD data for *J–R* tests of the beams precracked by uniform axial compression, reverse four-point bending and an uncracked specimen are shown in Figure 33. The beam without a precrack exhibited rapid, unstable growth when loads were increased to the point of crack initiation and gave no useful data for the FGM layers near the machined notch.

The specimen precracked by uniform axial compression showed stable crack growth with no pop-in during the *J–R* test indicating that a sharp crack was initiated during compressive loading. The load values and the resultant *J* values, however, were only 70% of those obtained by the specimen that was precracked with reverse four-point bending. The lower values for that specimen are due to extensive microcracking during application of the axial compressive loads. Figure 34 shows the *J* versus crack extension result for the reverse four-point bend precracked specimen (Carpenter *et al.*, 2000). The result demonstrates a rising *R*-curve behavior as the metal content increases in successive layers of the FGM.

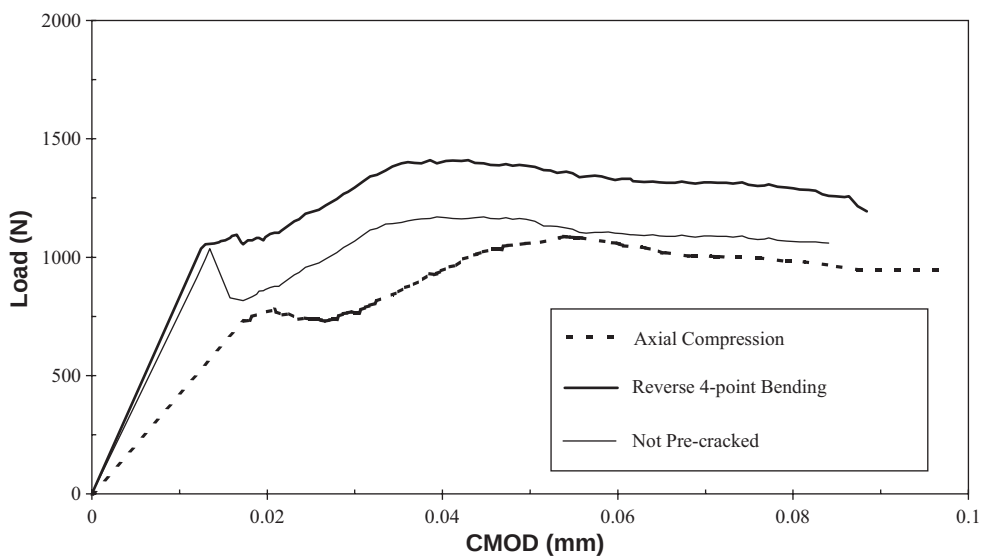

Figure 33 Load versus CMOD plot for Ti/TiB *J–R* tests (after Carpenter *et al.*, 2000).

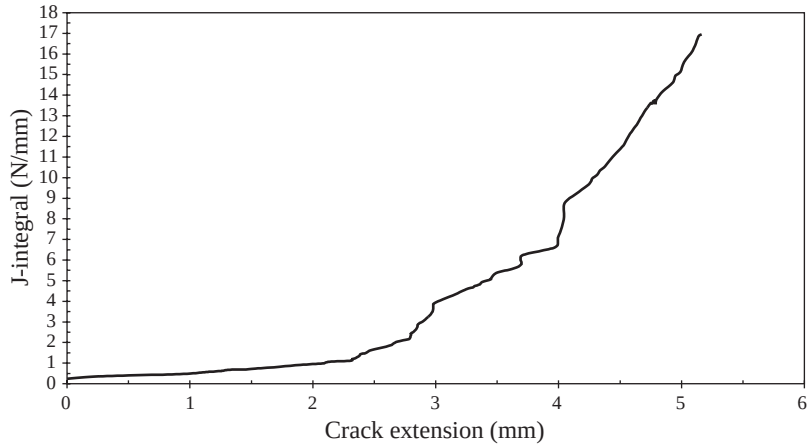

Figure 34 *J* versus crack extension plot for the Ti/TiB FGM (after Carpenter *et al.*, 2000).

2.13.6 CONCLUDING REMARKS AND PERSPECTIVES

Scientific research in FGMs considers, in a large sense, functions of gradients in materials comprising thermodynamic, chemical, mechanical, optical, electromagnetic, and/or biological aspects. The present work suggests a balanced approach involving modeling, synthesis, and experiments. It shows that our understanding on failure of FGMs is increasingly clear, however, it also indicates areas for future development such as investigation of constraint effects in fracture, full (i.e., for the entire range of material composition) experimental characterization of engineering FGMs under static and dynamic loading, development of fracture criteria with predictive capability, multiscale (space and time) failure considerations, and connection of research with actual industrial applications.

ACKNOWLEDGMENTS

This work was supported by the NASA-Ames "Engineering for Complex System Program," and the NASA-Ames Chief Engineer (Dr. Tina Panontin) through grant NAG 2-1424. Additional support for this work was provided by the National Science Foundation (NSF) under grant CMS-0115954 (Mechanics and Materials Program).

2.13.7 REFERENCES

J. Aboudi, M.-J. Pindera and S. M. Arnold, 1999, Higher-order theory for functionally graded materials. *Composites Part B: Eng.*, **30B**, 777–832.

R. Alex and L. Schovanec, 1996, An anti-plane crack in a nonhomogeneous viscoelastic body. *Eng. Fract. Mech.*, **55**, 727–735.

American Society for Testing and Materials, 1996, "Standard E1820-96," ASTM, Philadelphia, PA.

American Society for Testing and Materials, 1997, "PS 070-97," ASTM, West Conshohocken, PA.

T. L. Anderson, 1995, "Fracture Mechanics: Fundamentals and Applications," 2nd edn., CRC Press, Boca Raton.

G. Anlas, M. H. Santare and J. Lambros, 2000, Numerical calculation of stress intensity factors in functionally graded materials. *Int. J. Fract.*, **104**, 131–143.

R. Babaei and S. A. Lukasiewicz, 1998, Dynamic response of a crack in a functionally graded material between two dissimilar half planes under anti-plane shear impact load. *Eng. Fract. Mech.*, **60**, 479–487.

G. Bao and H. Cai, 1997, Delamination cracking in functionally graded coating/metal substrate systems. *Acta Mater.*, **45**, 1055–1066.

G. Bao and L. Wang, 1995, Multiple cracking in functionally graded ceramic/metal coatings. *Int. J. Solids Struct.*, **32**, 2853–2871.

T. L. Becker, Jr., R. M. Cannon and R. O. Ritchie, 2001, Finite crack kinking and T-stresses in functionally graded materials. *Int. J. Solids Struct.*, **38**, 5545–5563.

Y. Benveniste, 1987, A new approach to the application of Mori–Tanaka's theory in composite materials. *Mech. Mater.*, **6**, 147–157.

H. Cai and G. Bao, 1998, Crack bridging in functionally graded coatings. *Int. J. Solids Struct.*, **35**, 701–717.

G. T. Camacho and M. Ortiz, 1996, Computational modelling of impact damage in brittle materials. *Int. J. Solids Struct.*, **33**, 2899–2938.

R. D. Carpenter, W. W. Liang, G. H. Paulino, J. C. Gibeling and Z. A. Munir, 1999, Fracture testing and analysis of a layered functionally graded Ti/TiB beam in 3-point bending. *Mater. Sci. Forum*, **308–311**, 837–842.

R. D. Carpenter, G. H. Paulino, Z. A. Munir and J. C. Gibeling, 2000, A novel technique to generate sharp cracks in metallic/ceramic functionally graded materials by reverse 4-point bending. *Scr. Mater.*, **43**, 547–552.

E. M. Carrillo-Heian, R. D. Carpenter, G. H. Paulino, J. C. Gibeling and Z. A. Munir, 2001a, Dense layered $MoSi_2$/SiC functionally graded composites formed by field-activated synthesis. *J. Am. Ceram. Soc.*, **84**, 962–968.

E. M. Carrillo-Heian, C. Unuvar, J. C. Gibeling, G. H. Paulino and Z. A. Munir, 2001b, Simultaneous synthesis and densification of Niobium Silicide/Niobium composites. *Scr. Mater.*, **45**, 405–412.

Y.-S. Chan, G. H. Paulino and A. C. Fannjiang, 2001, The crack problem for nonhomogeneous materials under antiplane shear loading—a displacement based formulation. *Int. J. Solids Struct.*, **38**, 2989–3005.

Y.-S. Chan, A. C. Fannjiang and G. H. Paulino, 2003, Integral equations with hypersingular kernels—theory and applications to fracture mechanics. *Int. J. Eng. Sci.*, in press.

Y. F. Chen and F. Erdogan, 1996, The interface crack problem for a nonhomogeneous coating bonded to a homogeneous substrate. *J. Mech. Phys. Solids*, **44**, 771–787.

G. P. Cherepanov, 1967, Crack propagation in continuous media. *Prikl. Mat. Mekh. (Appl. Math. Mech.)*, **31**, 467–488.

G. P. Cherepanov, 1968, Cracks in solids. *Int. J. Solids Struct.*, **4**, 811–831.

H. J. Choi, 1996a, Bonded dissimilar strips with a crack perpendicular to the functionally graded interface. *Int. J. Solids Struct.*, **33**, 4101–4117.

H. J. Choi, 1996b, An analysis of cracking in a layered medium with a functionally graded nonhomogeneous interface. *ASME J. Appl. Mech.*, **63**, 479–486.

H. J. Choi, 2001a, The problem for bonded half-plane containing a crack at an arbitrary angle to the graded interfacial zone. *Int. J. Solids Struct.*, **38**, 6559–6588.

H. J. Choi, 2001b, Effects of graded layering on the tip behavior of a vertical crack in a substrate under frictional Hertzian contact. *Eng. Fract. Mech.*, **68**, 1033–1059.

H. J. Choi, K. Y. Lee and T. E. Jin, 1998a, Collinear cracks in a layered half-plane with a graded nonhomogeneous interfacial zone: Part I. Mechanical response. *Int. J. Fract.*, **94**, 103–122.

H. J. Choi, T. E. Jin and K. Y. Lee, 1998b, Collinear cracks in a layered half-plane with a graded nonhomogeneous interfacial zone: Part II. Thermal shock response. *Int. J. Fract.*, **94**, 123–135.

R. M. Christensen, 1971, "Theory of Viscoelasticity," Academic Press, New York.

R. D. Cook, D. S. Malkus and M. E. Plesha, 1989, "Concepts and Applications of Finite Element Analysis," 3rd edn., Wiley, New York.

B. Cotterell and J. R. Rice, 1980, Slightly curved or kinked cracks. *Int. J. Fract.*, **16**, 155–169.

S. Dag and F. Erdogan, 2002, A surface crack in a graded medium loaded by a sliding rigid stamp. *Eng. Fract. Mech.*, **69**(14–16), 1729–1751.

F. Delale and F. Erdogan, 1983, The crack problem for a nonhomogeneous plane. *ASME J. Appl. Mech.*, **50**, 609–614.

F. Delale and F. Erdogan, 1988, On the mechanical modeling of an interfacial region in bonded half-planes. *ASME J. Appl. Mech.*, **55**, 533–545.

G. J. Dvorak and J. Zuiker, 1994, The effective properties of functionally graded composites I. Extension of Mori–Tanaka method to linearly varying fields. *Composite Eng.*, **4**, 19–35.

J. W. Eischen, 1987a, Fracture of nonhomogeneous materials. *Int. J. Fract.*, **34**, 3–22.

J. W. Eischen, 1987b, An improved method for computing the J_2-integral. *Eng. Fract. Mech.*, **26**, 691–700.

F. Erdogan, 1978, Mixed boundary-value problems in mechanics. In: "Mechanics Today," ed. S. Nemat-Nasser, Pergamon, New York, vol. 4, pp. 1–86.

F. Erdogan, 1995, Fracture mechanics of functionally graded materials. *Composite Eng.*, **5**, 753–770.

F. Erdogan, G. D. Gupta and T. S. Cook, 1973, Numerical solution of singular integral equations. In: "Mechanics of Fracture," ed. G. C. Sih, Noordhoff, Leyden, vol. 1, pp. 368–425.

F. Erdogan, A. C. Kaya and P. F. Joseph, 1991, The crack problem in bonded nonhomogeneous materials. *ASME J. Appl. Mech.*, **58**, 410–418.

F. Erdogan and M. Ozturk, 1995, Periodic cracking of functionally graded coating. *Int. J. Eng. Sci.*, **33**, 2179–2195.

F. Erdogan and B. H. Wu, 1996, Crack problems in FGM layers under thermal stresses. *J. Thermal Stresses*, **19**, 237–265.

F. Erdogan and B. H. Wu, 1997, The surface crack problem for a plate with functionally graded properties. *ASME J. Appl. Mech.*, **64**, 449–456.

J. D. Eshelby, 1951, The force on an elastic singularity. *Phil. Trans. Roy. Soc.*, **A244**, 87–112.

L. Ewart and S. Suresh, 1986, Dynamic fatigue crack growth in polycrystalline alumina under cyclic compression. *J. Mater. Sci. Lett.*, **5**, 774–778.

A. Feng and Z. A. Munir, 1994, Field-assisted self-propagating synthesis of β-SiC. *J. Appl. Phys.*, **76**, 1927–1928.

A. Feng and Z. A. Munir, 1995a, The effect of an electric field on self-sustained combustion synthesis: Part I. Modeling studies. *Metall. Trans.*, **26B**, 581–586.

A. Feng and Z. A. Munir, 1995b, The effect of an electric field on self-sustained combustion synthesis: Part II. Field-assisted synthesis of β-SiC. *Metall. Trans.*, **26B**, 587–593.

T. Fett, D. Munz and Y. Y. Yang, 2000, Direct adjustment procedure for weight function analysis of graded properties. *Fatigue Fract. Eng. Mater. Struct.*, **23**, 191–198.

L. B. Freund, 1990, "Dynamic Fracture Mechanics," Cambridge University Press, Cambridge.

Y. C. Fung, 1965, "Foundations of Solid Mechanics," Prentice-Hall, Englewood Cliffs, New Jersey.

A. E. Giannakopoulos, S. Suresh, M. Finot and M. Olsson, 1995, Elastoplastic analysis of thermal cycling: layered materials with compositional gradients. *Acta Metall. Mater.*, **43**, 1335–1354.

W. A. Gooch, B. H. Chen, M. S. Burkins, R. Palicka, J. Rubin and R. Ravichandran, 1999, Development and ballistic testing of a functionally gradient ceramic/metal applique. *Mater. Sci. Forum*, **308–311**, 614–621.

P. Gu and R. J. Asaro, 1997a, Cracks in functionally graded materials. *Int. J. Solids Struct.*, **34**, 1–17.

P. Gu and R. J. Asaro, 1997b, Crack deflection in functionally graded materials. *Int. J. Solids Struct.*, **34**, 3085–3098.

P. Gu, M. Dao and R. J. Asaro, 1999, A simplified method for calculating the crack-tip fields of functionally graded materials using the domain integral. *ASME J. Appl. Mech.*, **66**, 101–108.

Z. Hashin and S. Shtrikman, 1963, A variational approach to the theory of the elastic behavior of multiphase materials. *J. Mech. Phys. Solids*, **11**, 127–140.

J. M. Herrmann and L. Schovanec, 1990, Quasi-static mode III fracture in a nonhomogeneous viscoelastic body. *Acta Mech.*, **85**, 235–249.

J. M. Herrmann and L. Schovanec, 1994, Dynamic steady-state mode III fracture in a nonhomogeneous viscoelastic body. *Acta Mech.*, **106**, 41–54.

R. Hill, 1965, A self-consistent mechanics of composite materials. *J. Mech. Phys. Solids*, **13**, 213–222.

T. Hirai, 1996, Functionally gradient materials. In: "Materials Science and Technology, Vol. 17B, Processing of Ceramics, Part 2," ed. R. J. Brook, VCH Verlagsgesellschaft mbH, Weinheim, Germany, pp. 292–341.

T. Hirano, J. Teraki and T. Yamada, 1990, On the design of functionally gradient materials. In: "Proceedings of the 1st International Symposium on Functionally Gradient Materials, Sendai, Japan, 1990," eds. M. Yamanouchi, M. Koizumi, T. Hirai and I. Shiota.

T. Honein and G. Herrmann, 1997, Conservation laws in nonhomogeneous plane elastostatics. *J. Mech. Phys. Solids*, **45**, 789–805.

G. R. Irwin, 1957, Analysis of stresses and strains near the end of a crack traversing a plate. *ASME J. Appl. Mech.*, **24**, 354–361.

B. Ilschner, 1996, Processing-microstructure-property relationships in graded materials. *J. Mech. Phys. Solids*, **44**, 647–656.

S. Itou, 2001, Transient dynamic stress intensity factors around a crack in a nonhomogeneous interfacial layer between dissimilar elastic half-planes. *Int. J. Solids Struct.*, **38**, 3631–3645.

Z.-H. Jin and R. C. Batra, 1996a, Some basic fracture mechanics concepts in functionally graded materials. *J. Mech. Phys. Solids*, **44**, 1221–1235.

Z.-H. Jin and R. C. Batra, 1996b, Stress intensity relaxation at the tip of an edge crack in a functionally graded material subjected to a thermal shock. *J. Thermal Stresses*, **19**, 317–339.

Z.-H. Jin and R. C. Batra, 1996c, Interface cracking between functionally graded coatings and a substrate under antiplane shear. *Int. J. Eng. Sci.*, **34**, 1705–1716.

Z.-H. Jin and R. C. Batra, 1998, *R*-curve and strength behavior of a functionally graded material. *Mater. Sci. Eng.*, **A242**, 70–76.

Z.-H. Jin and N. Noda, 1994a, Crack-tip singular fields in nonhomogeneous materials. *ASME J. Appl. Mech.*, **61**, 738–740.

Z.-H. Jin and N. Noda, 1994b, An edge crack in a nonhomogeneous material under thermal loading. *J. Thermal Stresses*, **17**, 591–599.

Z.-H. Jin and N. Noda, 1994c, Transient thermal stress intensity factors for a crack in a semi-infinite plane of a functionally graded material. *Int. J. Solids Struct.*, **31**, 203–218.

Z.-H. Jin and G. H. Paulino, 2001, Transient thermal stress analysis of an edge crack in a functionally graded material. *Int. J. Fract.*, **107**, 73–98.

Z.-H. Jin and G. H. Paulino, 2002, A viscoelastic functionally graded strip containing a crack subjected to in-plane loading. *Eng. Fract. Mech.*, **69**(14–16), 1769–1790.

Z.-H. Jin, G. H. Paulino and R. H. Dodds, Jr., 2002, Finite element investigation of quasistatic crack growth in functionally graded materials using a novel cohesive zone fracture model. *ASME J. Appl. Mech.*, **69**, 370–379.

S. Kadioglu, S. Dag and S. Yahsi, 1998, Crack problem for a functionally graded layer on an elastic foundation. *Int. J. Fract.*, **94**, 63–77.

R. Kaczmarek, W. Robert, J. Jurewicz, M. I. Boulos and S. Dallaire, 1984, Microprocessor control of the spraying of graded coatings. In: "Plasma Processing and Synthesis of Materials Symposium," eds. J. Szekely and D. Apelian. pp. 207–215, New York.

B. L. Karihaloo, 1982, On crack kinking and curving. *Mech. Mater.*, **1**, 189–201.

J.-H. Kim and G. H. Paulino, 2002, Finite element evaluation of mixed mode stress intensity factors in functionally graded materials. *Int. J. Numer. Methods Eng.*, **52**, 1903–1935.

K. Kokini and M. Case, 1997, Initiation of surface and interface edge cracks in functionally graded ceramic thermal barrier coatings. *ASME J. Eng. Mater. Technol.*, **119**, 148–152.

N. Konda and F. Erdogan, 1994, The mixed mode crack problem in a nonhomogeneous elastic medium. *Eng. Fract. Mech.*, **47**, 533–545.

J. Lambros, M. H. Santare, H. Li and G. H. Sapna III, 1999, A novel technique for the fabrication of laboratory scale model functionally graded materials. *Exp. Mech.*, **39**, 184–190.

Y.-D. Lee and F. Erdogan, 1995, Residual/thermal stresses in FGM and laminated thermal barrier coatings. *Int. J. Fract.*, **69**, 145–165.

C. Y. Li, G. J. Weng and Z. P. Duan, 2001, Dynamic behavior of a cylindrical crack in a functionally graded interlayer under torsional loading. *Int. J. Solids Struct.*, **38**, 7473–7485.

X. Ma, K. Tanihata, K. Miyamoto, Y. Kumakawa, S. Nagata, T. Yamada and T. Hirano, 1992, Fabrication of TiC/Ni functionally graded materials and their mechanical and thermal properties. *Ceram. Eng. Sci., Proc.*, **13**, 356–364.

A. J. Markworth, K. S. Ramesh and W. P. Parks, Jr., 1995, Modelling studies applied to functionally graded materials. *J. Mater. Sci.*, **30**, 2183–2193.

P. R. Marur and H. V. Tippur, 1998, Evaluation of mechanical properties of functionally graded materials. *J. Test. Eval.*, **26**, 539–545.

P. R. Marur and H. V. Tippur, 2000a, Dynamic response of bimaterial and graded interface cracks under impact loading. *Int. J. Fract*, **103**, 95–109.

P. R. Marur and H. V. Tippur, 2000b, Numerical analysis of crack-tip fields functionally graded materials with a crack normal to the elastic gradient. *Int. J. Solids Struct.*, **37**, 5353–5370.

S. A. Meguid, X. D. Wang and L. Y. Jiang, 2002, On the dynamic propagation of a finite crack in functionally graded materials. *Eng. Fract. Mech.*, **69**(14–16), 1753–1768.

Y. Miyamoto, K. Tanihara, Y. Matsuzaki and X. Ma, 1992, HIP in SHS technology. *Int. J. Self-Propagation High-Temp. Synth.*, **1**, 147–154.

T. Mori and K. Tanaka, 1973, Average stress in matrix and average elastic energy of materials with misfitting inclusions. *Acta Mater.*, **21**, 571–574.

Z. A. Munir, 1996, The use of an electric field as a processing parameter in the combustion synthesis of ceramics and composite. *Metall. Trans.*, **27A**, 2080–2085.

Z. A. Munir, 1997, Field effects in self-propagating solid state synthesis reactions. *Solid State Ionics*, **101**, 991–1001.

Z. A. Munir, W. Lai and K. Ewald, 1995, *US Patent* no. 5380409, January 10.

G. Nelson and A. Ezis, 1996, "Functionally graded material (FGM) armor in the TiB/Ti system (U)," CERCOM Report, Vista, CA 92083, USA.

M. Nemat-Alla and N. Noda, 2000, Edge crack problem in a semi-infinity FGM plate with a bidirectional coefficient of thermal expansion under two dimensional thermal loading. *Acta Mech.*, **144**, 211–229.

S. Nemat-Nasser and M. Hori, 1993, "Micromechanics: Overall Properties of Heterogeneous Materials," North-Holland, Amsterdam, The Netherlands.

N. Noda, 1999, Thermal stresses in functionally graded materials. *J. Thermal Stresses*, **22**, 477–512.

N. Noda and Z.-H. Jin, 1993, Thermal stress intensity for a crack in a strip of a functionally graded material. *Int. J. Solids Struct.*, **30**, 1039–1056.

R. M. Ogorkiewicz, 1970, "Engineering Properties of Thermoplastics," Wiley Interscience, London.

M. Ozturk and F. Erdogan, 1997, Mode I crack problem in an inhomogeneous orthotropic medium. *Int. J. Eng. Sci.*, **35**, 869–883.

M. Ozturk and F. Erdogan, 1999, The mixed mode crack problem in an inhomogeneous orthotropic medium. *Int. J. Fract.*, **98**, 243–261.

V. Parameswaran and A. Shukla, 1998, Dynamic fracture of functionally gradient material having discrete property variation. *J. Mater. Sci.*, **33**, 3303–3311.

V. Parameswaran and A. Shukla, 1999, Crack tip stress fields for dynamic fracture in functionally gradient materials. *Mech. Mater.*, **31**, 579–596.

V. Parameswaran and A. Shukla, 2002, Asymptotic stress fields for stationary cracks along the gradient in functionally gradient materials. *ASME J. Appl. Mech.*, **69**, 240–243.

G. H. Paulino and Z.-H. Jin, 2001a, Correspondence principle in viscoelastic functionally graded materials. *ASME J. Appl. Mech.*, **68**, 129–132.

G. H. Paulino and Z.-H. Jin, 2001b, Viscoelastic functionally graded materials subjected to antiplane shear fracture. *ASME J. Appl. Mech.*, **68**, 284–293.

G. H. Paulino and Z.-H. Jin, 2001c, A crack in a viscoelastic functionally graded material layer embedded between two dissimilar homogeneous viscoelastic layers – antiplane shear analysis. *Int. J. Fract.*, **111**, 283–303.

G. H. Paulino and J. H. Kim, 2003, The weak patch test for nonhomogeneous materials modeled with graded finite elements, submitted for journal publication.

M.-J. Pindera, J. Aboudi and S. M. Arnold, 1998, Thermomechanical analysis of functionally graded thermal barrier coatings with different microstructural scales. *J. Am. Ceramic Soc.*, **81**, 1525–1536.

I. S. Raju, 1987, Calculation of strain-energy release rates with high order and singular finite elements. *Eng. Fract. Mech.*, **28**, 251–274.

I. S. Raju and K. N. Shivakumar, 1990, An equivalent domain integral method in the two-dimensional analysis of mixed mode crack problems. *Eng. Fract. Mech.*, **37**, 707–725.

T. S. Ramamurthy, T. Krishmamurthy, K. B. Narayana, K. Vijayakumar and B. Dataguru, 1986, Modified crack closure integral method with quarter point elements. *Mech. Res. Commun.*, **13**(4), 179–186.

T. Reiter and G. J. Dvorak, 1998, Micromechanical models for graded composite materials: II. Thermomechanical loading. *J. Mech. Phys. Solids*, **45**, 1655–1673.

T. Reiter, G. J. Dvorak and V. Tvergaard, 1997, Micromechanical models for graded composite materials. *J. Mech. Phys. Solids.*, **45**, 1281–1302.

J. R. Rice, 1968, A path independent integral and approximate analysis of strain concentration by notches and cracks. *ASME J. Appl. Mech.*, **35**, 379–386.

C.-E. Rousseau and H. V. Tippur, 2000, Compositionally graded materials with cracks normal to the elastic gradient. *Acta Mater.*, **48**, 4021–4033.

C.-E. Rousseau and H. V. Tippur, 2001, Influence of elastic gradient profiles on dynamically loaded functionally graded materials with cracks along the gradient. *Int. J. Solids Struct.*, **38**, 7839–7856.

Y. A. Roy and R. H. Dodds, Jr., 2001, Simulation of ductile crack growth in thin aluminum panels using 3D surface cohesive elements. *Int. J. Fract.*, **110**, 21–45.

E. F. Rybicki and M. F. Kanninen, 1977, A finite element calculation of stress intensity factors by a modified crack closure integral. *Eng. Fract. Mech.*, **9**, 931–938.

M. Sakai and R. C. Bradt, 1993, Fracture toughness testing of brittle materials. *Int. Mater. Rev.*, **38**, 53–78.

M. H. Santare and J. Lambros, 2000, Use of graded finite elements to model the behavior of nonhomogeneous materials. *ASME J. Appl. Mech.*, **67**, 819–822.

N. Sata, 1993, Characteristics of SiC-TiB_2 composites as the surface layer of SiC–TiB_2–Cu functionally gradient material produced by self-propagating high-temperature synthesis. *Ceram. Trans.*, **34**, 109–116.

L. Schovanec and J. R. Walton, 1987a, The quasi-static propagation of a plane strain crack in a power-law inhomogeneous linearly viscoelastic body. *Acta Mech.*, **67**, 61–77.

L. Schovanec and J. R. Walton, 1987b, The energy release rate for a quasi-static mode I crack in a nonhomogeneous linearly viscoelastic body. *Eng. Fract. Mech.*, **28**, 445–454.

N. I. Shbeeb, W. K. Binienda and K. L. Kreider, 1999a, Analysis of the driving forces for multiple cracks in an infinite nonhomogeneous plate: Part I. Theoretical analysis. *ASME J. Appl. Mech.*, **66**, 492–500.

N. I. Shbeeb, W. K. Binienda and K. L. Kreider, 1999b, Analysis of the driving forces for multiple cracks in an infinite nonhomogeneous plate: Part II. Numerical solutions. *ASME J. Appl. Mech.*, **66**, 501–506.

C. F. Shih, H. G. de Lorenzi and M. D. German, 1976, Crack extension modeling with singular quadratic isoparametric elements. *Int. J. Fract.*, **12**, 647–651.

K. Suganuma, T. Okamoto, M. Koizumi and M. Shimada, 1984, Effect of interlayers in ceramic-metal joints with thermal expansion mismatches. *J. Am. Ceram. Soc.*, **67**, C256–C257.

S. Suresh and A. Mortensen, 1998, "Functionally Graded Materials," The Institute of Materials, IOM Communications, London.

I. Tamura, Y. Tomota and H. Ozawa, 1973, "Proceedings of the 3rd International Conference on Strength of Metals and Alloys," Institute of Metals, Cambridge, vol. 1, p. 611.

S. P. Timoshenko and J. N. Goodier, 1973, "Theory of Elasticity," McGraw-Hill, New York.

B. L. Wang, J. C. Han and S. Y. Du, 2000, Crack problems in nonhomogeneous composite subjected to dynamic loading. *Int. J. Solids Struct.*, **37**, 1251–1274.

X. Wang, Z. Zou and D. Wang, 1997, On the penny-shaded crack in a nonhomogeneous interlayer of adjoining two different elastic materials. *Int. J. Solids Struct.*, **34**, 3911–3921.

M. L. Williams, 1957, On the stress distribution at the base of a stationary crack. *ASME J. Appl. Mech.*, **24**, 109–114.

R. L. Williamson, B. H. Rabin and J. T. Drake, 1993, Finite element analysis of thermal residual stresses at graded ceramic-metal interfaces: Part I. Model description and geometrical effects. *J. Appl. Phy.*, **74**, 1310–1320.

H. Xue and Z. A. Munir, 1995, Extending the compositional limit of combustion synthesized B_4–TiB_2 composites by field activation. *Metall. Trans.*, **27**, 475–480.

H. Xue and Z. A. Munir, 1997, Synthesis of AlN-SiC composites and solid solution by field-activated self-propagating combustion. *J. Eur. Ceram. Soc.*, **17**, 1787–1792.

W. Yang and C. F. Shih, 1994, Fracture along an interlayer. *Int. J. Solids Struct.*, **31**, 985–1002.

J. R. Zuiker, 1995, Functionally graded materials: choice of micromechanics model and limitations in property variation. *Composite Eng.*, **5**, 807–819.

Comprehensive Structural Integrity
ISBN (set): 0-08-043749-4
Volume 2; (ISBN: 0-08-044156-4); pp. 607–644